TWO-PHASE FLOW EFFECT ON CARBONATE MATRIX ACIDIZING

A Dissertation

by

HAORAN CHENG

Submitted to the Office of Graduate and Professional Studies of
Texas A&M University
in partial fulfillment of the requirements for the degree of

DOCTOR OF PHILOSOPHY

Chair of Committee,	Ding Zhu
Committee Members,	A. Daniel Hill
	David Schechter
	Charles J. Glover
Head of Department,	A. Daniel Hill

December 2017

Major Subject: Petroleum Engineering

ABSTRACT

Matrix acidizing treatments are commonly used to improve the productivity of oil and gas wells in carbonate reservoirs. For a given volume of acid injection, the optimal injection rate can achieve the deepest wormhole penetration. Normally, the optimal condition is obtained through laboratory core flooding experiments with acid fluid injection into water saturated cores. However, in field treatments, acid fluid injected into oil and gas saturated formations creates a two-phase flow region. Two-phase flow effect on optimal treatment condition needs to be evaluated.

The research is conducted through experimental investigation and numerical modeling. In order to investigate two-phase flow effect in matrix acidizing, a systematic experimental study that covers a variety of back pressures, temperatures and injection rates is conducted. Computerized Tomography (CT) scan images are taken for each core sample after acid injection to evaluate the structures of the wormholes. With the experimental study, the effect of evolved CO_2 on wormhole propagation is examined. The test results show that at low injection rate, CO_2 present as a gaseous phase lowers wormhole propagation efficiency dramatically, and enlarged wormhole diameter is observed. This work verifies that two-phase flow affects the wormhole propagation.

A numerical model is developed to simulate two-phase flow effect on wormhole propagation. The model uses 3-D numerical simulation with two-scale continuum model and finite volume method to characterize matrix acidizing process. The model can capture both gravity effect and two-phase flow effect on wormhole propagation. From this

numerical model, we are able to estimate the properties that cannot be measured from lab experiment.

With the numerical model, we study the effect of several key factors, such as injection rate, viscosity, and residue non-wetting phase saturation on wormhole efficiency. The results show that wormhole propagation in two-phase flow region is quite different to single-phase flow. The presence of an immiscible phase, such as gas or oil, before acid injection, can increase the wormholing efficiency. The higher the oil viscosity, the lower volume of acid needed for wormhole penetrating the core. A higher initial saturation of oil, also reduces the breakthrough pore volume. High residue oil saturation has a positive effect on wormholing efficiency. It is important to investigate the effects and calibrate the lab results before using them in oil and gas reservoirs.

DEDICATION

Dedicated to my parents and my grandmother, for their love.

ACKNOWLEDGEMENTS

I would like to express my deepest gratitude to both Dr. Ding Zhu and Dr. Dan Hill for their supervision, guidance, and support on my research. Dr. Zhu is very patient and kind to me. She advised me not only on my research, but also on how to be a professional engineer. Dr. Hill is one of smartest people I have ever known. His immense knowledge leads me through some struggling times. I could not have imagined finishing this dissertation without their help.

I would also like to give my sincere gratitude to Dr. David Schechter for his advice during my research. Thanks also go to Dr. Charles Glover for serving on my committee and for his interest and patience on my research. His Transport Phenomena class provides me the fundamental knowledge for my study.

My gratitude also goes to my colleagues and friends, especially Mateus Schwalbert, Yuhai Zhou, Xiao Jin and Yoon Seok Sohn in matrix acidizing group for their help and discussion. I would also like to thank my colleagues in our research group. Time spent with them means a lot to me.

Thanks to John Maldonado for all his help with laboratory experiments.

Thanks also go to my friends at Texas A&M University. I will always remember the days with them.

Finally, I would like to thank my beloved parents and grandmother for their unconditional love and support.

CONTRIBUTORS AND FUNDING SOURCES

This work was supervised by a dissertation committee consisting of Professor Ding Zhu (advisor), Professor Dan Hill and Professor David Schechter of the Department of Petroleum Engineering and Professor Charles Glover of the Department of Chemical Engineering.

All work for the dissertation was completed by the student.

This work was made possible in part by the Acid Stimulation Research Program in Petroleum Engineering Department at Texas A&M University.

NOMENCLATURE

a_v	Solid rock specific surface area, m^{-1}
a_{v0}	Initial solid rock specific surface area, m^{-1}
C_b	Average acid concentration in wetting phase
C_p	Specific heat, BTU/lb °F
C_s	Acid concentration at rock surface
d	Diameter, m
D_m	Effective molecular diffusivity of acid, m^2/s
D_{eff}	Effective diffusivity coefficient, m^2/s
f_∞	Empirical number
g	Gravitational acceleration, m/s^2
J_{acid}	Acid flux, m/s
$\boldsymbol{K}_i$	Permeability tensor, m^2
K_0	Initial permeability, m^2
$\overline{\boldsymbol{K}}$	Mean permeability tensor, m^2
$\overline{\boldsymbol{K}}_H$	Mean permeability in horizontal direction, m^2
$\overline{\boldsymbol{K}}_V$	Mean permeability in vertical direction, m^2
$\overline{\boldsymbol{K}}_Z$	Mean permeability in z-direction, m^2
$\overline{K}_{max}$	Maximum value of three mean permeabilities, m^2
k_{ri}	i-phase relative permeability

k_{ramax}	Non-wetting phase endpoint relative permeability
k_{rbmax}	Wetting phase endpoint relative permeability
k_s	Surface reaction rate constant, m/s
k_c	Acid mass transfer coefficient, m/s
k_{eff}	Effective mass transfer coefficient, m/s
L	Length, m
L_i	i-phase gravitational contribution, s
m_n	Relative permeability parameter for non-wetting phase
m_w	Relative permeability parameter for wetting phase
m_{core}	Weight of the core holder, lb
M_{wet}	Wet weight, kg
M_{dry}	Dry weight, kg
M_i	i-phase mobility, m^3 s/kg
M_{HCl}	HCl molecular weight, kg/mol
M_{CO_2}	CO_2 molecular weight, kg/mol
p	Pressure, Pa
p_c	Capillary pressure, Pa
p_{c0}	Entry capillary pressure, Pa
q_{absorb}	Absorbed heat, BTU
q_{CO_2}	CO_2 injection rate, mL/min
q_{acid}	Acid fluid injection rate, mL/min

r_p	Pore radius, m
r_{p0}	Initial pore radius, m
Re_p	Pore scale Reynolds number
REV	Representative elementary volume
$R(C_s)$	Rate of acid consumption, m/s
S_i	Saturation of i-phase
S_a	a-phase saturation, non-wetting phase saturation
S_b	b-phase saturation, wetting phase saturation
S_{b0}	Initial wetting phase saturation
$S_{b,eff}$	Wetting phase effective saturation
$S_{b,irr}$	Irreducible wetting phase saturation
Sh	Sherwood number
Sh_∞	Typical Sherwood number
Sc	Schmidt number
$S(\varphi)$	Source term
S_p	Implicit part of source term
S_u	Explicit part of source term
t	Time, s
ΔT	Temperature difference, °F
u_{water}	Water attenuation coefficient
u_{voxel}	Voxel attenuation coefficient

V_{pore}	Pore volume, m^3
V_{bulk}	Bulk volume, m^3
V_{void}	Void volume, m^3
V_{REV}	Representative elementary volume, m^3
V_i	Volume occupied by i-phase, m^3
$\boldsymbol{U}_i$	Supercritical velocity, m/s
Z_n	Standard normally distributed random number

Greek

α	Pore size distribution index
ϕ	Porosity
ϕ_0	Original porosity
ϕ_{mean}	Mean porosity value
ϕ_e	Effective transport-through porosity
Φ	Global flux, m/s
Φ_p	Pressure gradient flux, m/s
Φ_g	Gravity flux, m/s
Φ_{pc}	Capillary pressure flux, m/s
δ	Dimensionless factor account for constrictivity
τ_f	Dimensionless factor account for tortuosity
β	Permeability evolution parameter

γ	Pore radius evolution parameter
η	Specific surface area evolution parameter
μ	Dynamic viscosity, kg/(m s)
ρ_i	i-phase density, kg/m^3
	CO_2 density, kg/m^3
	Water density, kg/m^3
	Gravimetric dissolving power
	Standard deviation of natural logarithm of porosity values
	Standard deviation of natural logarithm of permeability values
	stoichiometric coefficient

Subscripts

a	Non-wetting phase
b	Wetting phase
c	Solid phase, rock
$c \rightarrow f$	Cell center to face center

TABLE OF CONTENTS

Page

LIST OF FIGURES

Page

LIST OF TABLES

Page

1. INTRODUCTION

1.1 Background

In 2016, the total world natural gas production reached 3552 billion cubic meters and the total world natural gas consumption was 3543 billion cubic meters. The gas consumption increased by an average of 2.3% each year in the past ten years (BP, 2016). Due to the increasing demand for natural gas, gas reservoir development has been greatly valued. It is estimated that more than 40% of the world's gas reservoirs are carbonate reservoirs. Amongst all the different techniques deployed in carbonate reservoirs to increase gas well productivity, matrix acidizing is one of the oldest methods. Reactive acid is injected into the formation to dissolve carbonate rock and creates highly permeable channels called wormholes. In order to achieve the best productivity increase, wormholes bypass the damaged zone and penetrate deepest into the formation are preferred.

For a given volume of acid injection, optimal injection rate exists which creates the deepest wormhole penetration. Normally, the optimal condition is obtained through laboratory core flooding experiments. A wormhole efficiency curve is generated by curve fitting the experimental data using the Buijse-Glasbergen wormhole model (Buijse and Glasbergen, 2005). Although the optimal condition can be used for evaluating chemical effectiveness and field treatment design, the detailed reaction and wormhole propagation process cannot be revealed. Most lab matrix acidizing experiments are conducted with acid fluid injected into water saturated cores. In field treatments, acid is injected into gas- or oil-saturated formations creating a two-phase flow region around the wormhole which

may affect the wormhole propagation. Therefore, a two-phase matrix acidizing simulator is needed to evaluate the effect of two-phase flow on optimal treatment condition.

1.2 Literature review

Wormhole propagation process has been investigated by many researchers extensively in the past. Several main factors affecting wormhole patterns have been identified, and numerous experimental work has been done to investigate the effect of injection rate, temperature, pressure, reaction/diffusion, pore geometry, etc. Analytical and numerical models have also been developed to characterize wormhole propagation. In this section, some of the studies are reviewed.

1.2.1 Optimal conditions

Matrix acidizing process is characterized by wormhole efficiency. In numerous previous studies, different dissolution patterns were observed (Daccord, 1987; Hoefner and Fogler, 1989; Wang et al., 1993; Fredd and Fogler, 1999). **Fig. 1.1** shows the wormhole patterns under different injection rate (McDuff et al., 2010). When injection rate is low, a compact dissolution pattern is observed, in which acid dissolves a large amount of rock near the core sample inlet. When injection rate is intermediate, a dominant wormhole pattern is created. When the injection rate is high, ramified wormhole is generated. For a given volume of acid injection, there is an optimal injection rate (Wang et al., 1993) under which the deepest wormhole penetration can be achieved. As the pressure drop inside the

wormhole is negligible when compared with the pressure drop in the matrix over the same distance, the deepest penetration is preferred to yield the best stimulation results.

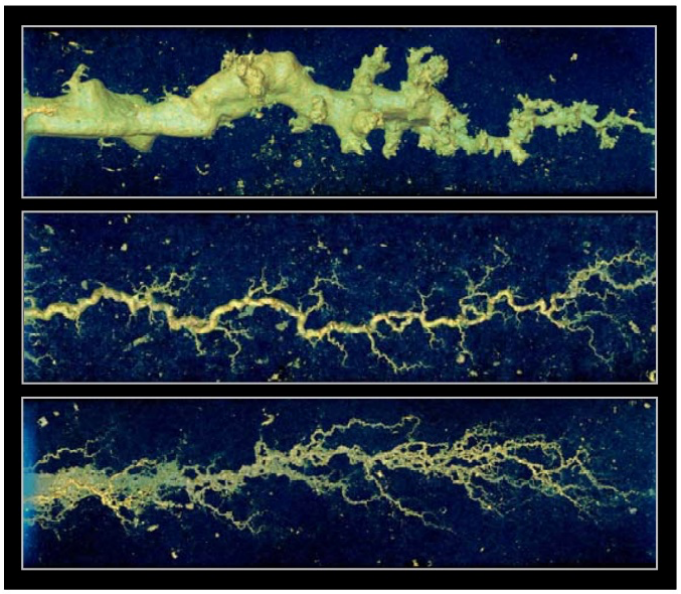

Figure 1.1 Dissolution pattern under different injection rates (McDuff et al., 2010)

Buijse and Glasbergen (Buijse and Glasbergen, 2005) developed a semi-empirical model to predict wormhole propagation. The model requires two input parameters: interstitial velocity of acid injection and breakthrough pore volume. These two parameters are obtained from laboratory experiments. Core flooding experimental data is curve fitted using the model to determine the optimal condition, as shown in **Fig 1.2**.

Gong and El Rabaa (Gong and El-Rabaa, 1999) developed a quantitative model to calculate optimal conditions using both Damköhler number and Peclet number. The model is based on Daccord et al.'s approach (Daccord et al., 1989). In order to account for all

acidizing dynamics in their model, several coefficients related to different reaction kinetics are introduced which makes the model very difficult to apply for treatment design.

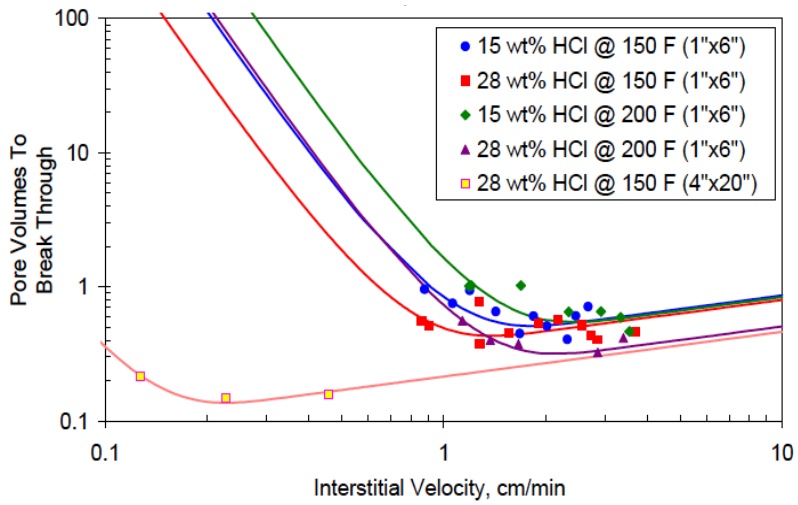

Figure 1.2 Experimental data curve fitted using Buijse and Glasbergen model (Furui et al., 2012)

Furui et al. (Furui et al., 2012) modified the Buijse and Glasbergen model based on computational fluid dynamic simulation and field data. In his model, he introduced two new parameters: wormhole tip velocity, which accounts for the core dimension effect, and wormhole axial-spacing coefficient. Through these parameters, he can upscale the core experimental results to the field scale. Based on his model, deeper wormhole penetration is predicted.

Among these models, the Buijse and Glasbergen model is still the most widely used model in matrix acidizing treatment design nowadays.

1.2.2 Mathematical models

Several numerical models for simulating wormhole propagation have been developed. The existing models can be categorized into four types: 1) the dimensionless parameter models; 2) the capillary tube models; 3) the network models, and 4) the two-scale continuum model. In this section, the existing models are briefly reviewed. Detailed reviews can be found in Schechter (Schechter, 1992), Golfier et al. (2002), Panga et al. (2005) and Akanni (2016).

1.2.2.1 The fractal and correlations models

The fractal and correlations models use some dimensionless groups, such as Damköhler number, Peclet number, kinetics, acid capacity number based on the correlations at the scale of the core sample to characterize experimental observation (Hoefner and Fogler, 1988; Daccord et al., 1993; Fredd and Fogler, 1998; C.N. Fredd and Fogler, 1999). Hoefner and Fogler (1988) initially studied the relationship between Damköhler number and different wormhole patterns. Fredd and Fogler (Fredd and Fogler, 1998) used Damköhler number to quantify wormhole propagation and reported optimal Damköhler number of 0.29 for different fluid/mineral systems, as shown in **Fig. 1.3**. However, a model of wormhole growth is needed to predict the optimal injection rate and the acid concentration effect is not considered.

1.2.2.2 The capillary tube models

In the capillary tube models, wormhole is treated as an existing cylindrical tube, and the transportation and reaction inside the wormhole are investigated (Schechter and Gidley,

1969; Hung et al., 1989; Buijse, 1997; Huang et al., 1997, 1999; Gdanski, 1999). From the model, the effect of fluid loss and reaction kinetics on wormhole propagation velocity is investigated. Wormhole population density can be predicted using the model. However, as the structure of the capillary tube model is simple, wormhole initiation and rock heterogeneities, as well as different dissolution patterns are not considered in these models.

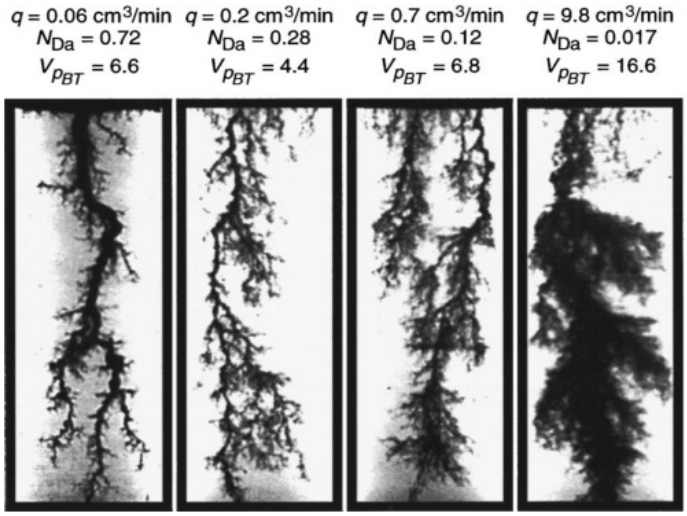

Figure 1.3 Wormhole structure at different Damköhler number (C N Fredd and Fogler, 1999)

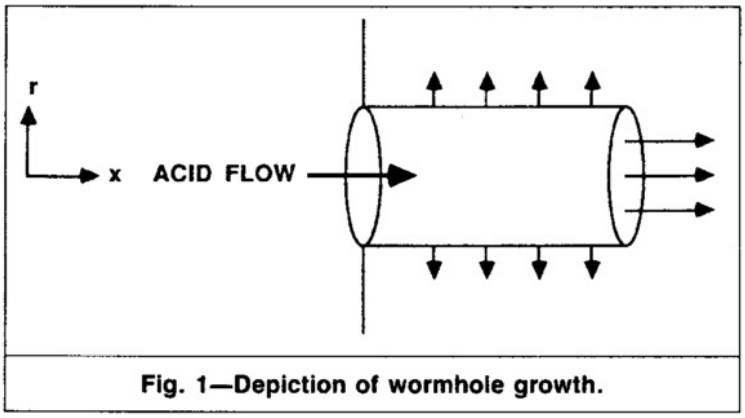

Figure 1.4 Schematic of capillary tube model (Hung et al., 1989)

1.2.2.3 The network models

Network model was used to simulate acid reaction during wormhole propagation (Hoefner and Fogler, 1989; Fredd and Fogler, 1998). The network model represents the porous medium as a network of capillary tubes interconnected to each other at the nodes (**Fig. 1.5**). The dissolution process is characterized by increased radius of the capillary tube. The dissolution rate is assumed to be proportional to the average velocity and acid concentration in the tube. The network model can capture the dissolution patterns qualitatively, however, the simulation results of breakthrough pore volume are much higher than experimental results and the computational power required by this model is enormous when upscale to laboratory scale.

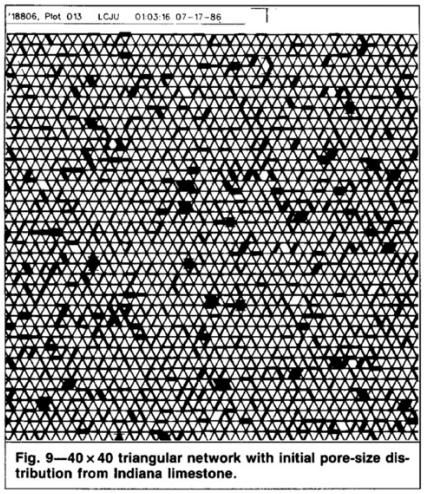

Fig. 9—40 × 40 triangular network with initial pore-size distribution from Indiana limestone.

Figure 1.5 Network model (Hoefner and Fogler, 1989)

1.2.2.4 The two-scale continuum models

The matrix acidizing process consists of two different processes in two different scales, the acid transport in porous media at the Darcy scale and acid/rock reaction at the pore scale, as shown in **Fig. 1.6**. The continuum model or averaged volume model was first introduced by Anderson and Jackson (1967) and Marle (1982). A weighting function was used for volume averaging. Quintard and Whitaker (1999) adopted the method in solving the problem of dissolution of an immobile phase in porous media. The advantage of continuum model is that it describes dissolution at the Darcy scale. The continuum is larger than pore scale, but smaller than core scale. In the continuum, all the properties inside the control volume are averaged and pore scale processes such as rock dissolution can be related and transferred to the Darcy scale.

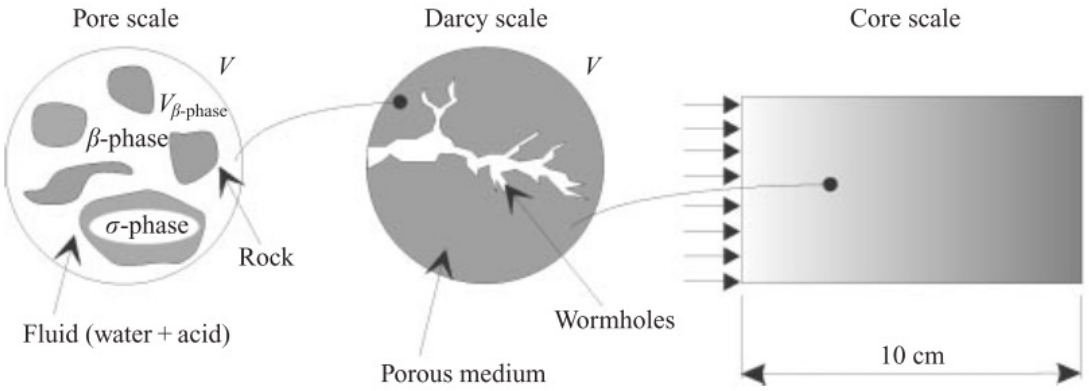

Figure 1.6 Different scale of the problem (Golfier et al., 2002)

Liu and Ortoleva (1996) developed a two-dimension two-scale continuum geochemical simulator based on the numerical solution of the equations which coupled multiphase fluid flow, species transport, energy balance and rock/fluid reactions. It also accounts for the effects of grain growth/dissolution and alteration of porosity and permeability. He studied the acidizing in sandstone and acetic acidizing in carbonate. The model was only valid in reaction-rate dominated dissolution.

Golfier et al. (2001, 2004) developed a Darcy-scale model to simulate carbonate matrix acidizing, which extended Liu's (1996) work. The model coupled the pore scale model to the Darcy scale. It assumed mass transfer dominated flow regime during the acidizing process.

Panga et al. (2005) studied the dissolution patterns capturing both reaction dominated and mass transfer dominated mechanism, extended the previous work. The model is applicable to linear flow simulation and can be used to investigate the effect of reaction kinetics, dispersion and mass transfer.

Kalia et al. (2007, 2009) extended Panga's model into radial flow. They studied the effect of porous medium heterogeneities on dissolution patterns. In their model, porosity field was populated uniformly by adding a random magnitude fluctuation to the mean value of the porosity. Liu et al. (2013) used normal distribution to generate porosity. They claimed that simulation results were much closer to experimental results than that obtained from the uniform distribution and the normally distributed porosity was more reasonable. Maheshwari et al. (2013) extended the model to three-dimension.

Additional work was done by De Oliveira et al. (2012) to investigate the effect of mineralogical heterogeneity on optimal acid injection rate. Ratnakar et al. (2012) used the model to investigate the effect of gelled acid accounting viscosity as a function of shear rate, pH, and temperature. Akanni et al. (2016) extended the work to simulate wormhole propagation by organic acids and chelating agents. They also classified the existing models into seven categories and discussed the application and shortcomings (Akanni and Nasr-El-Din, 2015).

Soulaine and Tchelepi (2016) proposed a modeling framework using the Darcy-Brinkman-Stokes equation instead of the Darcy's equation to describe the flow inside the wormhole and the surrounding porous medium. The framework can be extended to other applications related to two-scale continuum modeling. Schwalbert et al. (2017) implemented the framework to investigate the effect of anisotropy in carbonate reservoir. They concluded that in anisotropic reservoirs, the wormholes tended to align with the direction of maximum permeability and different injection volume may be needed compared to isotropic reservoirs.

1.2.3 Two-phase flow effect on wormhole propagation

Although there are several models for wormhole propagation simulation, few of them account for two-phase flow effect. In real field application, there are several scenarios that two-phase flow phenomena can be involved in the wormholing process, such as injecting gas with acid, evolved gas during acidizing treatment, or acid injection into oil and gas formations.

Ward (1986) studied using N_2 and CO_2 to create energized and foamed acid system. His results showed that foamed acid improves the treatment results in two major factors that it reduced acid reaction rate and fluid loss.

Hoefner et. al. (1987) conducted acid in oil emulsion tests for carbonate acidizing. The results showed improved wormhole propagation. They concluded that the acid in oil emulsion created micro-emulsions, reduced acid diffusivity and created less branching wormholes.

Bernadiner et. al. (1992) investigated the effect of foams on carbonate acidizing. Nitrogen and acid were injected commingled into the surfactant saturated core. Foam was generated during acidizing. Their study showed that wormhole produced under foam presence displayed little branching. They also conducted a test with no surfactant injected, in which no foam generated. Higher wormhole efficiency than only acid injection was observed. They concluded that the increase in efficiency was attributed to reduced fluid loss due to relative permeability.

Shukla et. al. (2003) conducted a series of experiments with nitrogen injected before acid injection. They discovered that with nitrogen injected ahead of acid, the

breakthrough pore volume for wormhole decreased by factors of 1.5 to 3. The wormholes were narrower and less branching compared to the ones without gas preconditioning. They concluded that a high saturation of gas phase in the acid system could enhance wormhole propagation. They also reported when gas and acid injections were alternated, wormholes became more branched and more acid was required for wormhole propagation.

Qiu et al. (2013, 2014) studied the effect of the back pressure of core-flood apparatus on wormhole propagation. They measured acid diffusion coefficient under different pressure. In their experiment, when the experiments were conducted at lower pressure (1000 psi), the presence of CO_2 significantly increased the wormhole diameter and slowed the wormhole propagation. They concluded that gaseous CO_2 had a negative impact on wormhole propagation.

1.3 Objective and approach

In field acidizing treatments, acid injected into oil or gas formations creates a two-phase region around the wormhole. The effect of two-phase flow on wormhole propagation needs to be investigated in order to better design the treatments. As most laboratory experiments and numerical simulator for determining optimal conditions have not taken two-phase effect into consideration, detailed experiments and a numerical simulator accounting for two-phase flow effect are the tasks of this study.

This study aims at 1) investigate the evolved CO_2 effect on wormhole propagation; 2) study the effect and possible factors of two-phase flow on wormhole propagation. We carry out the study both experimentally and numerically.

In the experimental study, core flooding experiments are conducted to examine the effects of evolved CO_2 on wormholing behavior. The experiments are conducted at both room temperature and an elevated temperature. Different backpressures from 500 to 3,000 psi are applied in the experiments. The Buijse and Glasbergen (2005) model is used for curve fitting to obtain the optimal acid injection rate and optimal pore volume to breakthrough for each experiment. Computed-tomography (CT) scan images are taken for each core sample after acid injection to evaluate the structures of the wormholes.

In the modeling work, a 3-dimensional two-phase core-scale matrix acidizing simulator is developed. Implicit Pressure Explicit Saturation (IMPES) method is used for two-phase flow simulation. The Brooks and Corey relative permeability and capillary pressure models are used for the effective properties calculation. The two-scale continuum model and finite volume method are implemented to represent the porous medium dissolution process. The simulation model is then used to predict wormhole propagation, and the results are compared with the experimental observations.

1.4 Dissertation outline

In this dissertation, Chapter 1 gives the background of this research by literature review. The objectives and approaches are stated.

In Chapter 2, the experimental setup is described, with detailed explanations of experimental procedures and CT image processing. In Chapter 3, we present the experimental results and discussions on evolved CO_2 effect on wormhole propagation. In Chapter 4, a 3-D two-phase matrix acidizing numerical simulator is developed. The method used to solve the model is described and the model is validated. Chapter 5 presents

the simulation of evolved CO_2 effect and the parametric study results for two-phase flow effect. Chapter 6 gives the conclusions based on the results and discussion of the study.

2. EXPERIMENTS ON EVOLVED CARBON DIOXIDE EFFECT

2.1 Introduction

Hydrochloric acid (HCl) is commonly used for carbonate acidizing treatments. In order to determine the optimum injection rate for HCl under different conditions and different rocks, laboratory core flooding experiments are conducted. When HCl is injected into carbonate rocks (calcite), the following reaction occurs:

$$CaCO_3 + 2HCl \rightarrow CaCl_2 + H_2O + CO_2 \quad (2\text{-}1)$$

CO_2 is one of the products generated in the reaction. At laboratory conditions, 1000 psi backpressure is commonly used for acidizing experiments to keep CO_2 in the solution. However, on the basis of the solubility of CO_2 in water, 1000 psi is not enough to keep CO_2 in solution. **Fig. 2.1** shows the solubility of carbon dioxide in calcium chloride-water solution at 75°C. According to Prutton's research (Prutton and Savage, 1945), even for the solutions containing only 10% calcium chloride, a pressure of over 600 atm (8817 psi) was needed in order to dissolve completely the evolved CO_2 in the solution. Generally, the acid used for acidizing is 15 wt% HCl, which would result in the formation containing about 25 wt% calcium chloride. In such a case, undissolved CO_2 in the spent acid region can present as another phase in the system. Because the properties of CO_2 change with pressure and temperature, the evolution of CO_2 and its effect on wormhole propagation efficiency need to be investigated to evaluate optimal acid-injection conditions accurately.

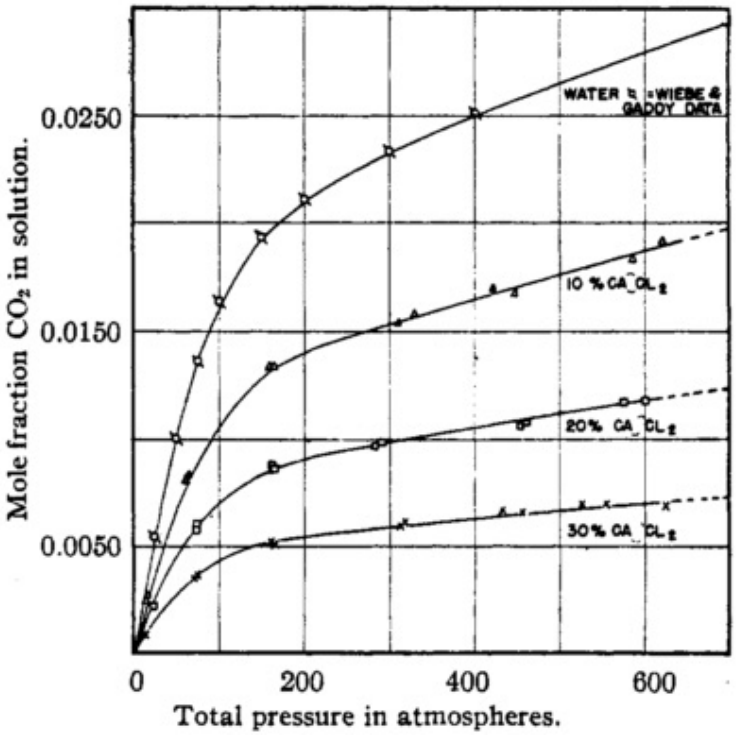

Figure 2.1 CO_2 solubility at 75°C (Prutton and Savage, 1945)

2.2 Experimental setup

This section provides an overview of the experimental setup (section 2.2.1) and detailed introduction of specific equipment (section 2.2.2-2.2.7)

2.2.1 Experimental setup overview

The matrix acidizing experimental setup schematic for this research is shown in **Fig. 2.2**. The apparatus comprises a pumping system, an accumulation system, a core holder, a pressure-maintain system, a heating system and a data-acquisition system. The details of the setup can be found in Grabski's work (Grabski, 2012).

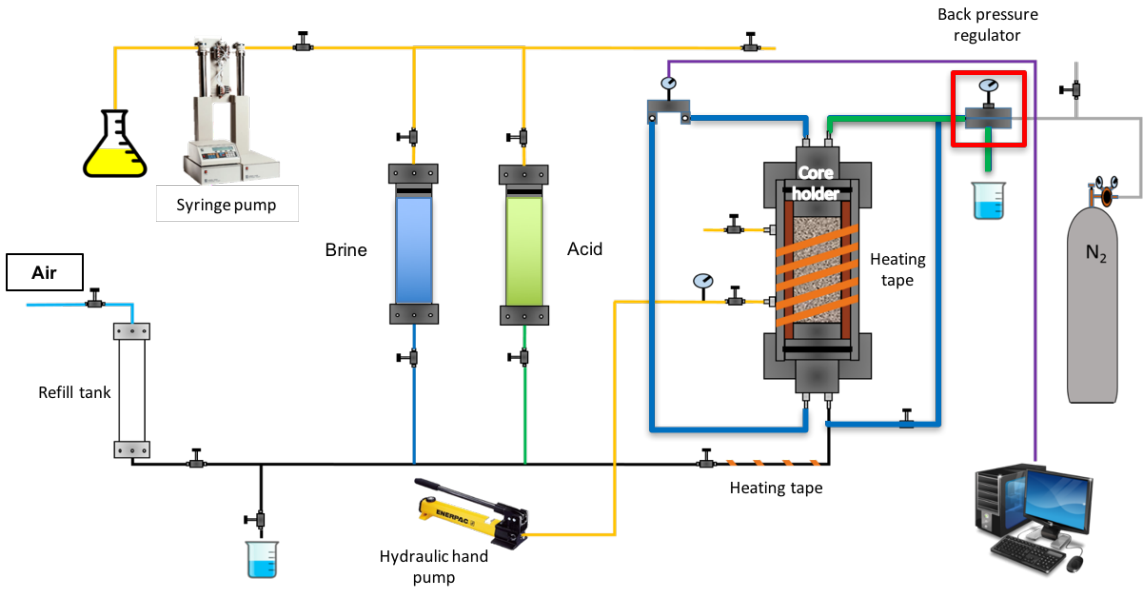

Figure 2.2 Experimental setup schematic

2.2.2 Pumping system

The pumping system consists two Teledyne ISCO syringe pump, as shown in **Fig. 2.3**. Two pumps are connected to generate continuous flow at a certain flow rate. The pump can provide injection rate from 0.0001mL/min to 107 mL/min. The maximum operating pressure allowed is 7,000 psi. For safety concern, the maximum pressure is set at 5500 psi. Hydraulic oil is used as the displacement fluid. During the experiment, to achieve continuous injection, the maximum injection rate is 45 mL/min.

Figure 2.3 Teledyne ISCO syringe pump

2.2.3 Accumulation system

The accumulation system consists of two accumulators and one refill tank, as shown in **Fig. 2.4**. Accumulators are used for storing brine and acid during experiments and prevent the pump from contacting corrosive fluids. The accumulators are made by Phoenix Instruments. The capacity of the accumulator is 1000 mL, and the maximum pressure rating is 5000 psi. The water accumulator is made of stainless steel 316, and the acid accumulator is made of Hastelloy C276.

There is a piston inside of the accumulator that separate the hydraulic mineral oil and injection fluid (brine or acid). During injection, syringe pump injects hydraulic oil from the top of the accumulator, which pushes the piston downward, and the piston displaces the injection fluid into the flow tubing.

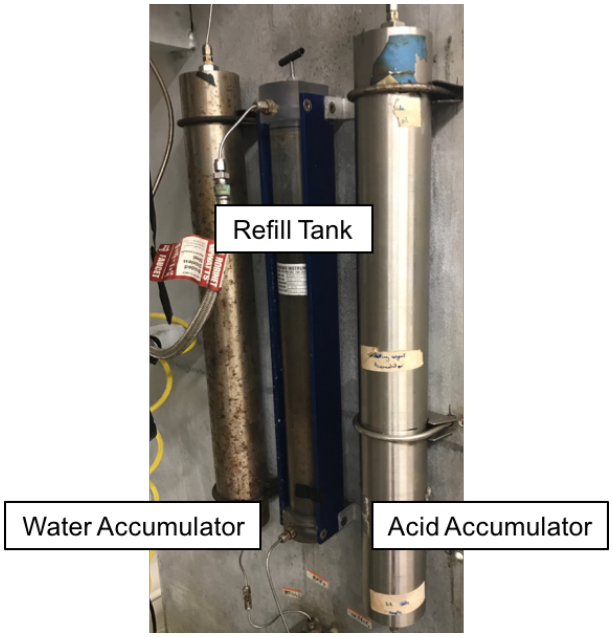

Figure 2.4 Accumulation system

The refill tank is located between two accumulators. It is made of PVC, which is acid resistant. The capacity of the refill tank is 1000 mL. The refill tank provides a way to refill fluid to both accumulators. For example, if brine accumulator needs to be refilled, brine is poured into the refill tank. Air is pumped from the top of the refill tank through the yellow pipe and pushes the brine into the water accumulator.

2.2.4 Core holder

The core holder, as shown in **Fig. 2.5** is made of Hastelloy C276. It is manufactured by Phoenix Instruments with a maximum pressure rating of 5000 psi and a maximum temperature rating of 300°F. It can hold cores with the size of 1.5-inch in diameter and a maximum length of 20 inches. There is a Viton sleeve inside the core holder. Hydraulic

oil is pumped into the space between the sleeve and the inner wall of the core holder to provide a confining pressure to the core.

The core holder consists of four parts: the main body (**Fig. 2.5**), the inlet plug (**Fig. 2.6a**), the outlet plug (**Fig. 2.6b**), the outlet cap (**Fig. 2.6c**). The main body has two connections; one serves as the hydraulic oil inlet, the other one serves as a release valve for releasing confining pressure when needed. The inlet plug has two tubing connected, one is for fluid injection, the other is connected to pressure transducer high-pressure port. The length of the inlet plug can be adjusted by taking out the metal spacers. The outlet plug has two tubing connected, one for fluid out flow and the other is connected to the pressure transducer lower port. The outlet cap is placed on the top of outlet plug to secure the plug-in position. When assembling the core holder, first, plug in the inlet plug from the bottom of the core holder and turn until the position is secure. Then, plug in the outlet plug. After that, put on the outlet cap, screw the top nob in until the outlet plug contacts the core. Continue screw to add about 10 psi pressure on the core.

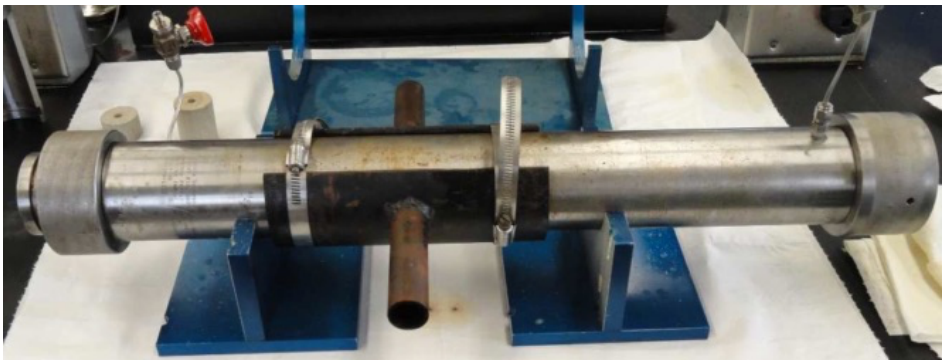

Figure 2.5 Core holder

Figure 2.6 Core holder part: (a) inlet plug, (b) outlet plug, (c) inlet cap

2.2.5 Pressure-maintain system

Pressure-maintain system consists of two parts: 1) hydraulic hand pump for maintaining confining pressure; 2) back pressure regulator for maintaining the lowest pressure of the system.

The hydraulic hand pump, as shown in **Fig. 2.7**, is manufactured by Enerpac. The model number is P-392, The maximum pressure rating is 10,000 psi, and usable oil capacity is 900 mL. The pump can provide 2.5 mL oil displacement per stroke. When experiment starts, the hand pump is used for pumping hydraulic oil into the space between the Viton sleeve and core holder. It provides confining pressure to the core and prevents fluid bypass the core. The confining pressure is kept 400-500 psi higher than the injection pressure.

Figure 2.7 Hydraulic hand pump Enerpac P-392 (Enerpac)

The backpressure regulator, as shown in **Fig. 2.8**, is manufactured by Equilibar. The model number is EB1HP1-HC276. Its maximum pressure rating is 5000 psi. The regulator is made of Hastelloy C276.

Figure 2.8 Backpressure regulator (Equilibar)

The internal structure of the backpressure regulator is shown in **Fig. 2.9**. The backpressure regulator consists of three main parts: the cap, the diaphragm, and the body. A nitrogen tank with gauge is used as the manual pressure regulator and connected to the

cap. Inlet and outlet are connected to the body. The PTFE diaphragm is in the middle. When applying backpressure, nitrogen is filled in the cap and presses down the diaphragm, the inlet and outlet are sealed. Only when the inlet pressure exceeds the pressure added on the diaphragm, fluid can push up the diaphragm, and then the inlet and outlet are connected. In this case, fluid can flow from inlet to outlet. **Fig. 2.10** shows the detailed schematic of each part of the backpressure regulator.

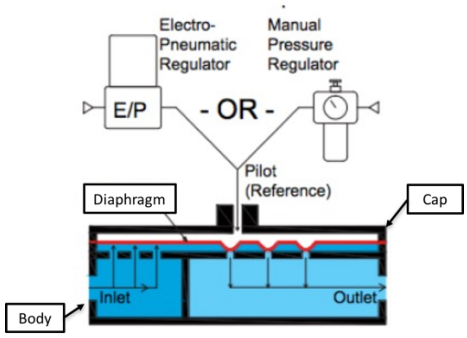

Figure 2.9 Backpressure regulator internal structure (Equilibar)

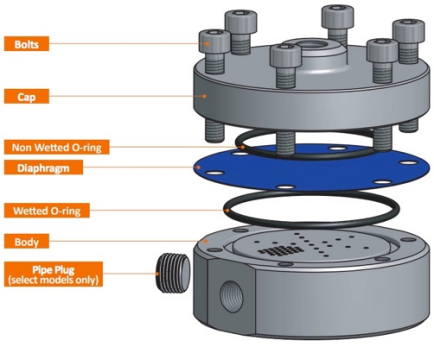

Figure 2.10 Detailed schematic of each part of backpressure regulator (Equilibar)

Backpressure regulator is the key apparatus for this study. It controls the minimum pressure of the system. During the experiment, different backpressure is applied to the backpressure regulator.

2.2.6 Heating system

Two heating tapes are used for heating both the core holder and the fluid. The heating tape, as shown in **Fig. 2.11**, is manufactured by Omega. Comparing with other heating methods, heating tape allows direct contact to the heating element, improving heat transfer efficiency and easy to install for each experiment.

In order to achieve a maximum temperature of 250 °F, a rough calculation is made to determine the required power for the heating tape. The specific heat capacity for limestone is 0.217 BTU/(lb °F), for Hastelloy C276 is 0.102 BTU/(lb °F). Use limestone specific heat for calculation. The weight of the core holder is 30 lb and an 8-inch core is 1.5 lb. If heating the core from 70 °F to 250 °F in one hour, the power needed for the heating tape can be calculated as:

The heat needs to be absorbed in one hour

$$q_{absorb} = mC_p(\Delta T) = \left(30\ lb \times \frac{0.102\ BTU}{\text{lb °F}} + 1.5\ \text{lb} \times \frac{0.217\ BTU}{\text{lb °F}}\right) \times (250 - 70)°\text{F}$$

$$= 609.39\ \text{BTU} \qquad (2\text{-}2)$$

where m is the weight of the core and core holder, C_p is the specific heat for limestone, ΔT is the temperature difference need to achieve.

The heating power needed for the heating tape when using a safety factor of 20% is

$$Power = \frac{q_{absorb}}{3.412\left(\frac{BTU}{watt\ hr}\right)}(1 + 20\%) = \frac{609.39\ BTU}{3.412\left(\frac{BTU}{watt\ hr}\right)} \times 1.2 = 214.32\ watt/hr \quad (2\text{-}3)$$

Figure 2.11 Heating tape

2.2.7 Data acquisition system

The data acquisition system consists of four components: the pressure transducers, the thermocouples, an NI signal processing board and a computer with LabVIEW software.

Two Foxboro differential pressure transducer (**Fig. 2.12**) are used for pressure acquisition. One transducer has a pressure range of 0-200 psi and the other one has the pressure range of 0-2000 psi. There are two ports on the lower part of the transducer which are connected to the inlet and outlet for the core holder respectively. The transducer measures the differential pressure of the inlet and outlet of the core holder. A diaphragm inside the transducer is deflected base on the pressure differential and converts the deflection into an electronic signal. The electronic signal is sent through the National

Instruments signal processing board to the computer. A LabVIEW program is used for pressure monitoring and recording during the experiment.

Figure 2.12 Foxboro pressure transducer

2.3 Core flooding experimental procedure

The experiments are conducted with Indiana limestone cores (**Fig. 2.13**). All cores are 1.5-inch in diameter and 8-inch in length to eliminate core size effects (Dong et al, 2014). The average porosity of the core samples is 14%, and the average permeability is 10 md, detailed properties of each core sample can be found in **Table 3.3**. The acid used in this study is a 15 wt% solution of HCl with 0.3 vol% common commercial corrosion inhibitor. All the experiments comprise a permeability test, a matrix acidizing treatment and a CT scan process.

Figure 2.13 Indiana limestone core sample 1.5 inch by 8 inch

Before the experiment, the cores are dried in the oven for 8 hours. Dry weight is measured from the cores. After that, cores are saturated in the saturation cell (**Fig. 2.14**). A vacuum pump (**Fig. 2.15**) is used to vacuum the saturation cell for 8 hours to make sure they are fully saturated with water. Wet weight is measured after the saturation process.

Figure 2.14 Saturation cell

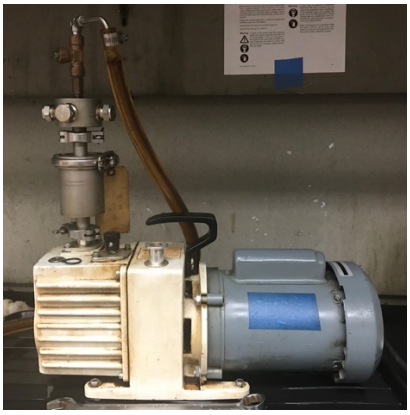

Figure 2.15 Vacuum pump

porosity is calculated using dry weight and wet weight of the core by the following equations:

$$\phi = \frac{V_{pore}}{V_{bulk}} \times 100\% \quad (2\text{-}4)$$

$$V_{pore} = \frac{M_{wet} - M_{dry}}{\rho_{water}} \quad (2\text{-}5)$$

$$V_{bulk} = \frac{1}{4}\pi d^2 L \quad (2\text{-}6)$$

where ϕ is porosity, V_{pore} is pore volume, V_{bulk} is bulk volume of the core, M_{wet} is the wet weight, M_{dry} is the dry weight, ρ_{water} is the density of the water, d is core diameter, L is core length.

During an experiment, the system is pressurized first by injecting water. Confining pressure is applied using a hydraulic hand pump to make sure the fluids does not bypass the core, and the pressure is kept at 400 to 500 psi higher than the injection pressure. Once the flow reaches steady state, the pressure drop across the core is recorded through the differential pressure transducer. The permeability is calculated using the Darcy's Law

from the measured pressure difference across the core holder. The system is then heated for the experiments with elevated temperature. When the system, including both the fluid and the core holder, reaches the desired temperature, water injection is switched off, and acid injection starts. Injection is stopped when wormholes break through the core (pressure drop across the core reaches zero), and the acid injection time is recorded for break-through-pore-volume calculation.

The effect of evolved CO_2 on optimal wormholing condition is examined by varying two parameters: temperature and pressure. Eight sets of experiments are conducted. Four sets of experiments are run at room temperature, and four sets of experiments are run at 150°F. Both at room temperature and at elevated temperature, the pressure effect is examined by setting the backpressure regulator to four different values: 500; 1,000; 2,000 and 3,000 psi. Forty tests are conducted during the study for the purpose of generating wormhole-efficiency curves. For each set of experiments, four to six tests are conducted with the same condition except the injection rate (interstitial velocity) until the optimal condition is identified. The Buijse-Glasbergen model (Buijse and Glasbergen, 2005) is used to generate the wormhole-efficiency relationship by fitting the experimental data. The experimental conditions are summarized in **Table 2.1**.

Table 2.1 Summary of experimental conditions

Experimental set	*Temperature (°F)*	*Pressure (psi)*	*Number of Runs*
1	70	500	4
2	70	1000	6
3	70	2000	6
4	70	3000	6
5	150	500	5
6	150	1000	4
7	150	2000	4
8	150	3000	5

2.4 Wormhole structure 3D visualization

After the matrix acidizing experiments, X-ray Computed-tomography (CT) scan is used to obtain images of the wormholes after each experiment. The apparatus used in this study is Toshiba Aquilion RXL 16-decetor CT system, as shown in **Fig 2.16**.

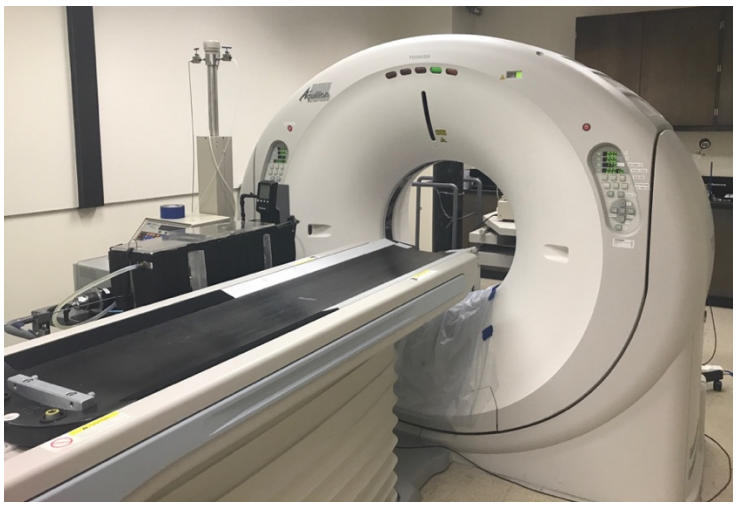

Figure 2.16 CT scanner

During CT scan process, the core sample is sent to the CT scanner in the axial direction. The sample is divided into multiple slices with a constant thickness and is scanned by X-rays at radial direction. Each slice is then converted into 3D voxels containing CT number. CT number is related to energy attenuation of the x-ray beam. The attenuation is related to electron density and atomic number of the materials present in the object being scanned. Each material possesses a distinct linear attenuation coefficient, and the total response received by the detectors is a combination of these coefficients (Izgec, 2009). By convention, CT number is calculated as

$$\text{CT number (in Hounsfield units, HU)} = 1000\,\frac{(u_{voxel}-u_{water})}{u_{water}} \tag{2-7}$$

where u_{voxel} is the calculated voxel attenuation coefficient, u_{water} is the attenuation coefficient of water. Higher density and higher atomic numbers result in higher attenuation of X-rays. Thus, in this study, rock grain is detected as voxels with high CT number and pore space containing air is detected as voxels with low CT number. A wormhole is detected as connected voxels with low CT number.

The dataset is imported to an open source DICOM image viewer: Horos. The general procedure for processing the CT image is as followed:

1. Import files to Horos
2. Open the image set
3. Use the oval tool to select region of interest (ROI)
4. Propagate ROI
5. Set the pixel values outside of the ROI as “3024”
6. Click “3D volume rendering”

7. Adjust histogram value to show wormhole structure

8. Save the wormhole image and video

Through the software, 3D wormhole images are generated and wormhole morphology is examined.

Fig. 2.17 shows the image files imported into Horos. **Fig. 2.18** shows the reconstructed wormhole structure image.

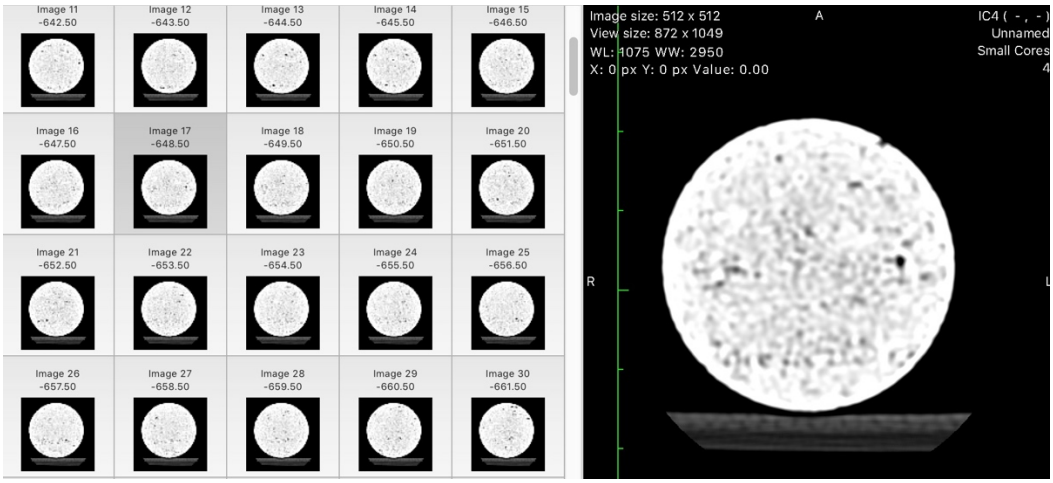

Figure 2.17 Image files imported into Horos

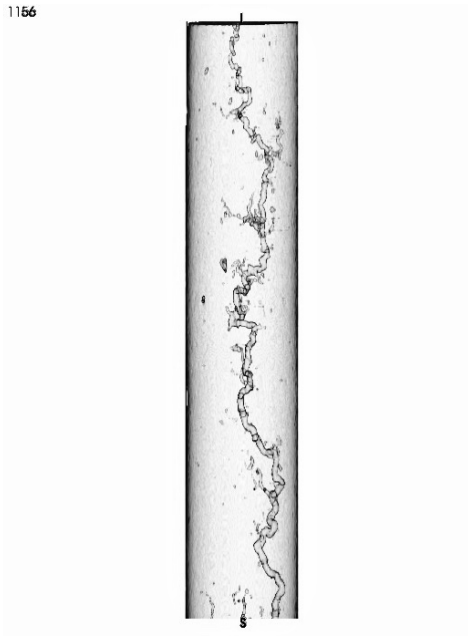

Figure 2.18 Example of reconstructed wormhole structure image

3. EXPERIMENTAL RESULTS AND DISCUSSION*

In this section, the results of core-flood experiments are shown for low-temperature tests and elevated-temperature tests, and the effect of CO_2 present as another phase is discussed.

3.1 Room temperature results

Figure. 3.1 shows the wormhole-efficiency relationship for four sets of experiments conducted at the backpressure settings of 500; 1000; 2000; and 3000 psi at the room temperature (70 °F). The markers are experimental results, and the curves are results fitted using the Buijse and Glasbergen (2005) model. From **Fig. 3.1**, we can see that the level of backpressure has no significant impact the optimal conditions for the backpressures from 1,000 to 3,000 psi; the curves are overlapping. The optimal conditions are very close to each other for all three backpressure values. Under the backpressure of 500 psi, the wormhole propagation behavior is fundamentally different from the results at the backpressures of 1000 psi and higher. At the lowest injection rate, which yields an interstitial flux of approximately 0.6 cm/min, the pore volumes to breakthrough are approximately four times higher than those observed at the higher backpressures. Perhaps more interestingly, the breakthrough pore volume response as a function of interstitial flux does not follow the normal Buijse and Glasbergen model. In fact, at 500 psi backpressure,

*Part of this section is reprinted with permission from "Cheng, H., Zhu, D. & Hill, A.D., 2016. The Effect of Evolved CO_2 on Wormhole Propagation in Carbonate Acidizing: SPE Production & Operations, (February), pp.24–26. Further reproduction prohibited without permission. Available at: http://www.onepetro.org/doi/10.2118/178962-MS.

the breakthrough pore volume monotonically decreases as interstitial flux increases, with no minimum observed over the range of the flow rates tested. The acid efficiency for the 500 psi backpressure experiments, particularly at low flow rates, can be understood by examining the morphology of the wormholes created. **Fig. 3.2** shows the CT scan images of wormhole generated at the flow rate of 1.5 mL/min at different back pressures. Wormhole created at 500 psi backpressure is much larger in diameter than those created at 1000 psi or higher backpressures, explaining the much higher acid consumption observed in the 500 psi back pressure experiments.

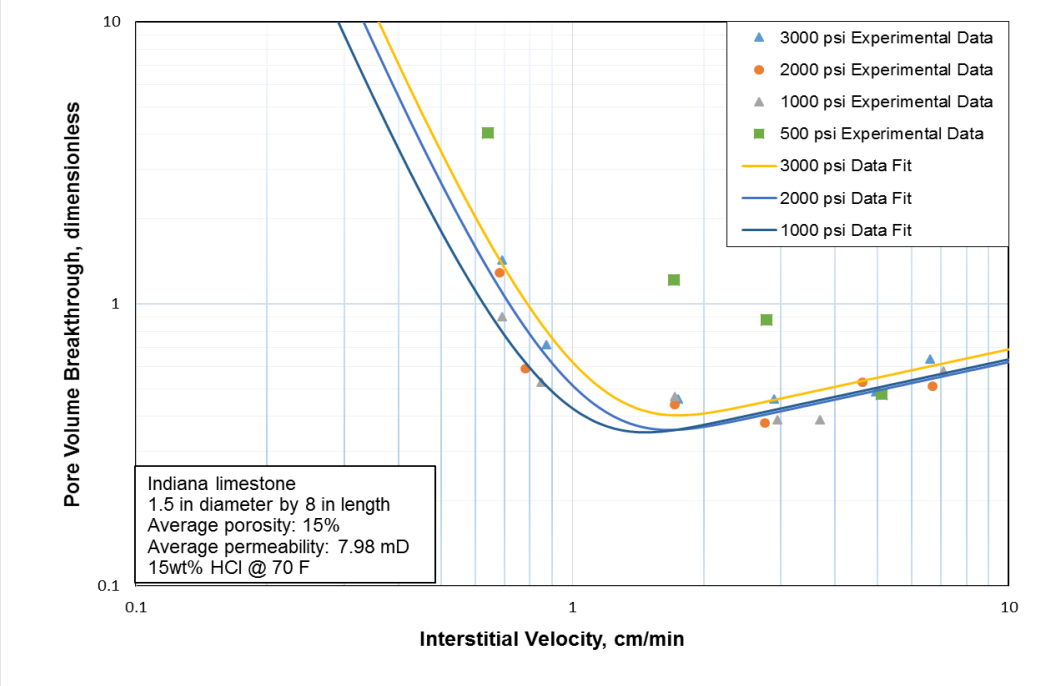

Figure 3.1 Wormhole efficiency relationship at 70°F

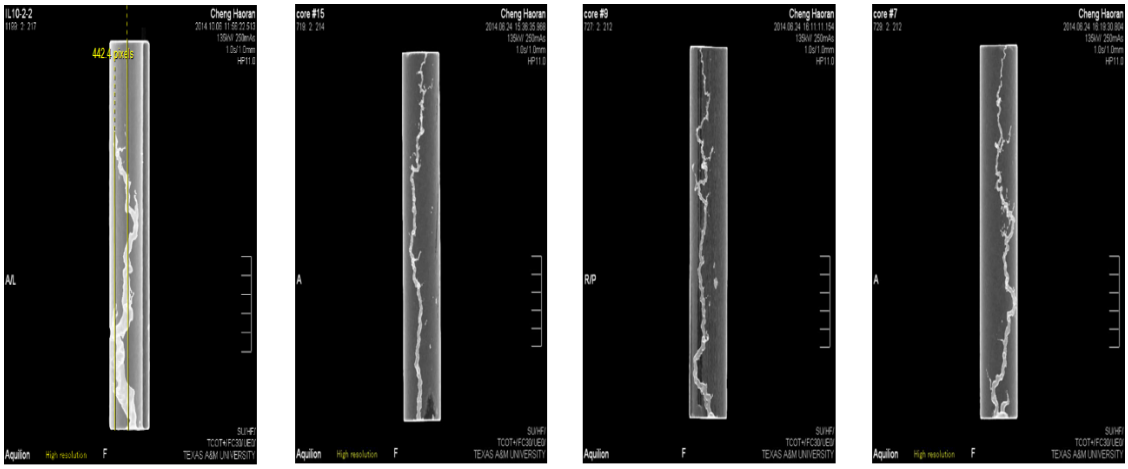

Figure 3.2 CT scan images for 1.5 mL/min injection rate (interstitial velocity = 0.7 cm/min) at 70°F

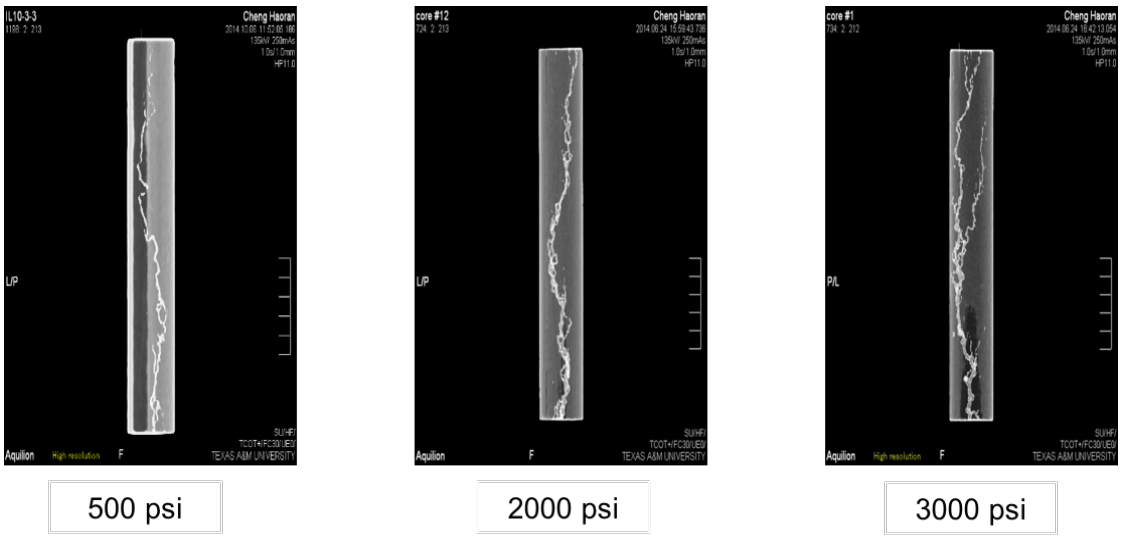

Figure 3.3 CT scan images for 8 mL/min injection rate (interstitial velocity = 7 cm/min) at 70°F

During the wormhole propagation process, rock dissolution happens in two places: the wormhole tip and the wormhole wall. At low injection rate, the dissolution volume on the wormhole wall consumes higher portion of acid than that at high injection rate. The extreme case is that the acid chemical is all consumed by the wormhole wall, resulting no acid chemical transported to the wormhole tip, wormhole cannot propagate and face dissolution occurs. Thus, larger wormhole diameter is expected when injection rate is low. However, in this case, extremely large wormhole diameter is observed at 500 psi backpressure, low injection rate. This observation indicates more dissolution occurs on wormhole wall comparing with that at higher backpressure. Acid chemical transport to wormhole tip at this backpressure is hindered.

The CO_2 pressure/temperature diagram shown in **Fig. 3.4** further explains the different wormholing behavior at 500 psi backpressure compared with 1000 psi or higher backpressure at room temperature (70°F). At this temperature and 500 psi backpressure, undissolved CO_2 present as a gaseous phase, at greater than 1000 psi, undissolved CO_2 present as a liquid phase. For the same amount of CO_2 generated, gaseous phase CO_2 with lower density occupies much higher volume. The pressure profile with a generated wormhole in the core is shown in **Fig. 3.5** (Dong, 2015). The pressure after the wormhole tip is equilibrium, with the same value as that in the wormhole. Thus, the generated CO_2 will flow inside the wormhole with acid flux, as illustrated in **Fig. 3.6**. At low injection rate, CO_2 present as gaseous phase may accumulate and cause local gas block slowing down acid transport inside the wormhole, as illustrated in **Fig. 3.7**. On the contrary, liquid CO_2 has much lower impact on acid fluid transportation. Fresh acid can reach wormhole

tip with less obstacles and wormhole propagation is not largely slowed down at higher backpressure.

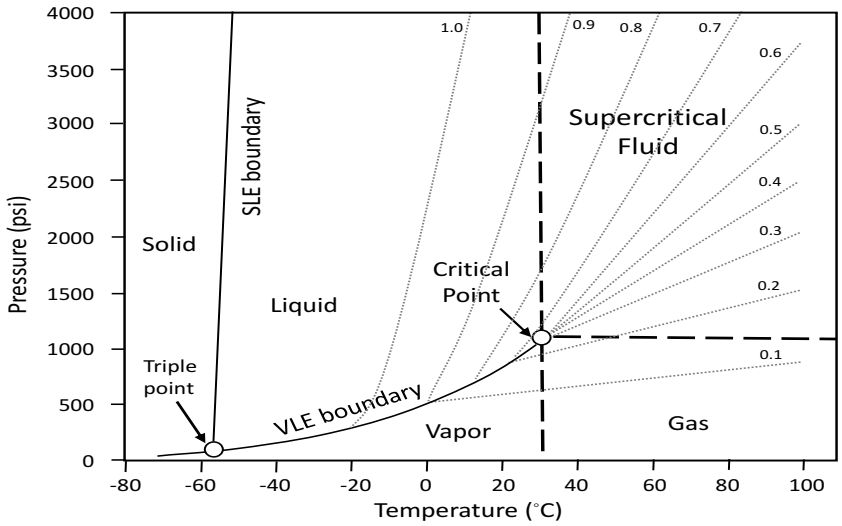

Figure 3.4 Pressure/temperature diagram for CO_2. (SLE = solid/liquid equilibrium; VLE = vapor/liquid equilibrium)

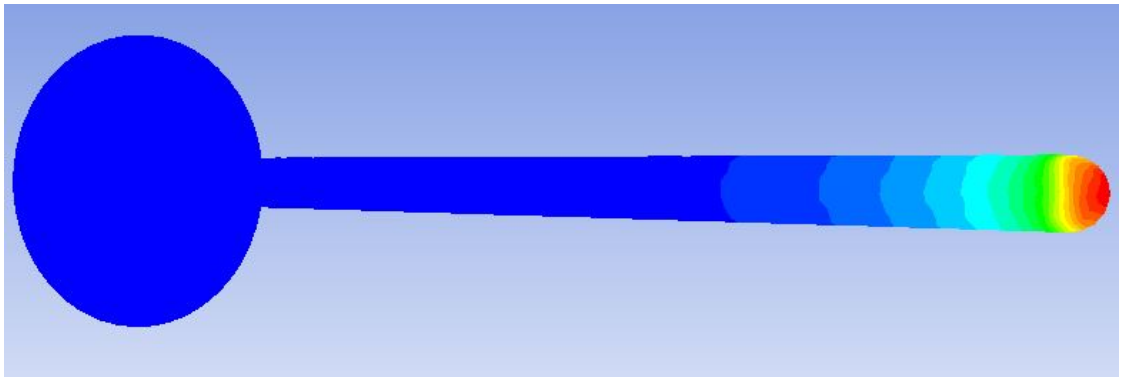

Figure 3.5 Pressure profile with generated wormhole (Dong, 2015)

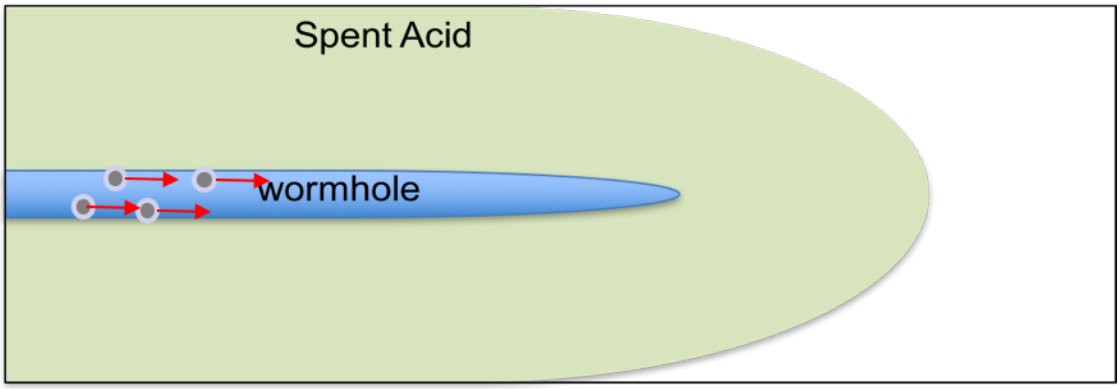

Figure 3.6 Illustration of CO_2 flow in wormhole

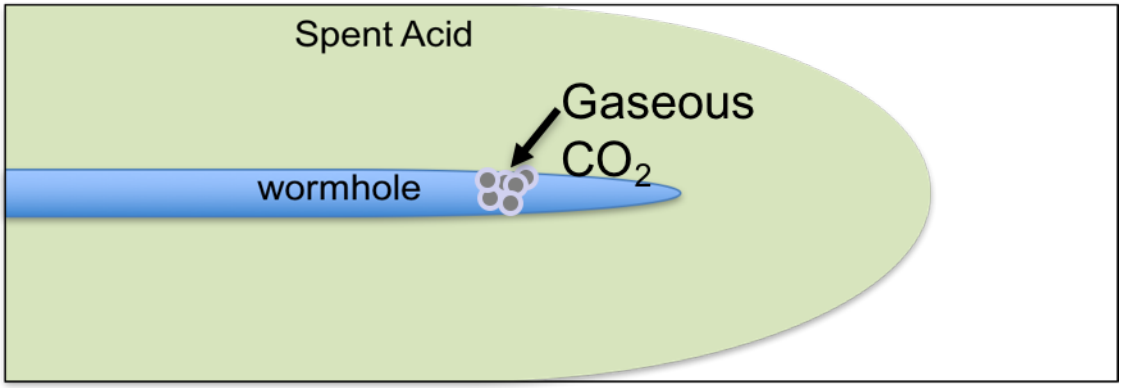

Figure 3.7 Illustration of gaseous CO_2 block acid transport at low injection rate

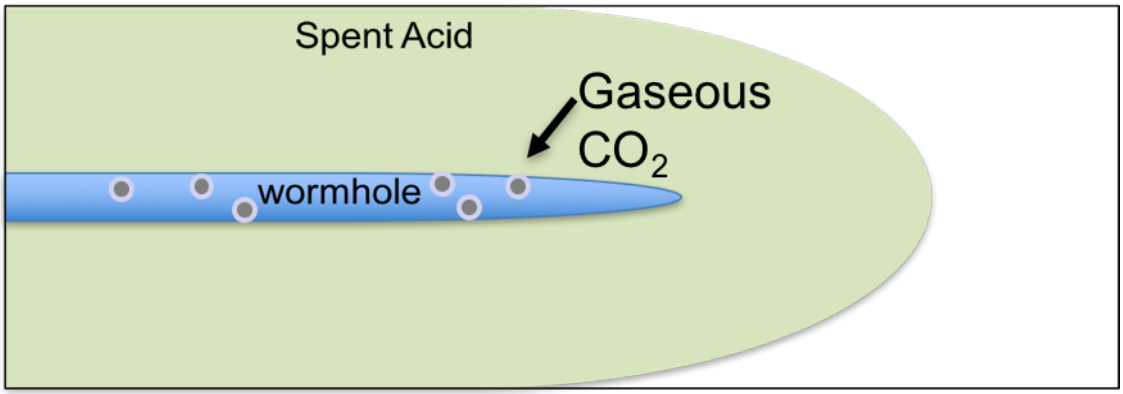

Figure 3.8 Illustration of gaseous CO_2 disperse in acid fluid at high injection rate

As the injection rate is increased, the wormhole propagation rate at low pressure behaves more and more like that at higher pressures. At the highest injection rate, at which the interstitial flux is approximately 7 cm/min, the acid consumption to propagate a wormhole through a core at low pressure is almost identical to that at higher pressures, and the wormhole structures are similar (**Fig. 3.3**). Apparently, at higher injection rates, generated gaseous CO_2 may disperse as little bubbles in the acid fluid and is less likely to accumulate and block the wormhole propagation, as illustrated in **Fig. 3.8**. The gaseous CO_2 has less and less effect as the injection rate increases. It is important to note that the conditions of 70°F temperature and 500 psi backpressure are not likely to exist at downhole in carbonate reservoirs. The primary utility of these results is to provide guidelines for relevant laboratory testing of acid systems in carbonate rocks. The optimal conditions for the room-temperature experiments are listed in **Table 3.1**

Table 3.1 Optimal conditions from experimental results at 70°F

Back Pressure (psi)	Optimal Interstitial Velocity (cm/min)	Optimal Breakthrough pore volume
500	-	-
1000	1.56	0.34
2000	1.70	0.35
3000	1.78	0.34

3.2 Elevated temperature results

As the reservoir temperature is normally higher than 70°F, we examine the effect of CO_2 on wormholes propagating at an elevated temperature. The room temperature experiments are repeated, but with the system heated to 150ºF. **Fig. 3.9** shows four sets of experimental results for wormhole efficiency at 150ºF. Four different backpressure values (500; 1000; 2000; and 3000 psi) are applied to the system. From **Fig. 3.9**, we can see that when the backpressure is set at 2000 and 3000 psi, there are no significant differences in the wormhole efficiency curves. With backpressures of 500 and 1000 psi, the acidizing-efficiency curve could also be fitted with the Buijse and Glasbergen model, but the optimal flux is almost two to three times higher than that observed at the backpressures of 2000 or 3000 psi. The CT-scan images of the wormholes created at low injection rate (**Fig. 3.10**) show a low efficiency, conical wormhole at 1000 psi backpressure, but near-optimal wormholes at backpressures of 2000 and 3000 psi. At the highest injection rate tested, the wormholes created with all four backpressures are very similar (**Fig. 3.11**).

The CO_2 pressure/temperature diagram (**Fig. 3.4**) again helps to explain the differences in the wormholing behavior observed. At 150ºF (66ºC), below the CO_2-phase-transition pressure (1074 psi), such as at 500 or 1000 psi, CO_2 is in the gaseous phase just below the boundary with supercritical fluid. At greater than 1074 psi, such as at 2000 and 3000 psi, CO_2 is a supercritical fluid. CO_2 density and viscosity properties as a function of pressure under different temperatures are plotted in **Fig. 3.12**. From the plot, we can see that the differences in the CO_2 properties at less than and greater than 1074 psi at 150ºF

are not as great as the differences between CO_2 properties at 500 and 1000 psi or higher at 70ºF, and the effects on wormhole behavior are also lower.

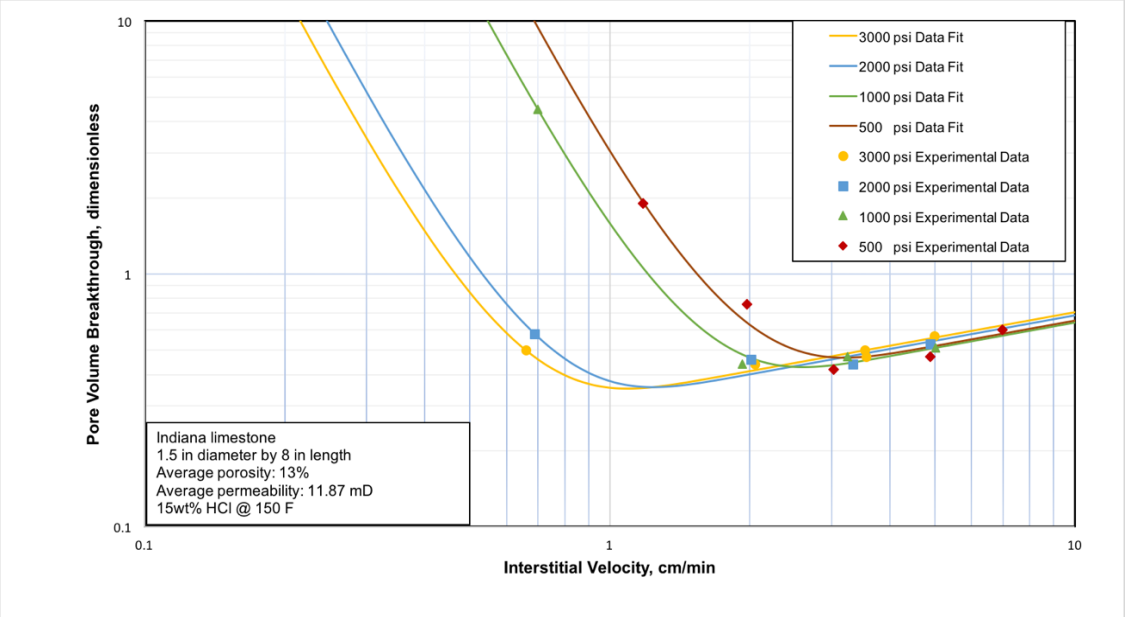

Figure 3.9 Wormhole efficiency relationship at 150°F

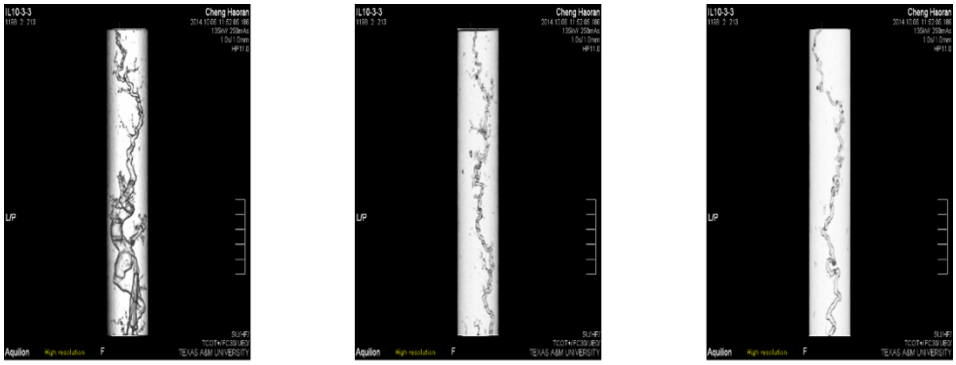

Figure 3.10 CT scan images for 1 mL/min injection rate (interstitial velocity = 0.66 cm/min) at 150°F

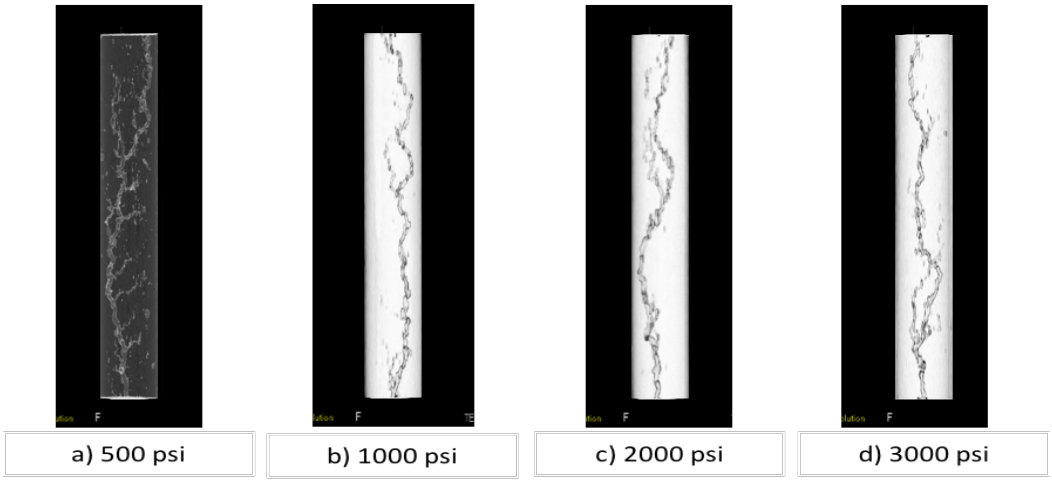

Figure 3.11 CT scan images for 8 mL/min injection rate (interstitial velocity = 7 cm/min) at 150°F

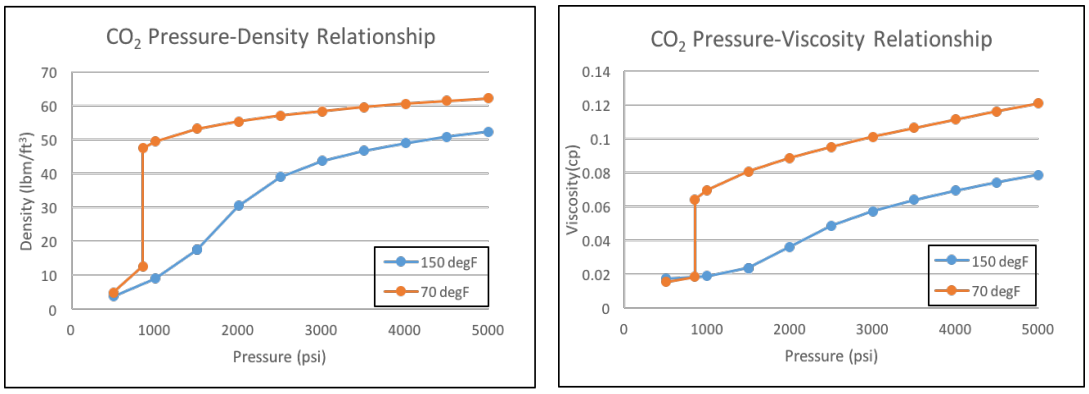

a) b)

Figure 3.12 CO_2 properties under different pressures and temperatures: (a) CO_2 density and (b) CO_2 viscosity.

The optimal interstitial velocities and pore volumes to breakthrough for the elevated-temperature experiments are listed in **Table 3.2**.

Table 3.2 Optimal conditions from experimental results at 150°F

Back Pressure (psi)	Optimal Interstitial Velocity (cm/min)	Optimal Breakthrough pore volume
500	3.26	0.45
1000	2.6	0.41
2000	1.26	0.34
3000	1.11	0.34

The optimal theory of wormhole propagation has been long accepted by the industry. For field treatments, it is recommended to inject at a rate at least equal to or greater than the optimal injection rate for longer wormhole penetration. When the injection rate is lower than the optimal rate, wormholes propagate much slower. This study shows that when gaseous CO_2 exists in the system because of low pressure, wormhole-propagation rate is reduced significantly. The negative impact increased breakthrough pore volume up to eight times in the experiments conducted in this study. To avoid the negative impact of gaseous CO_2, it is critical to keep the injection rate at greater than the optimal condition. The complete experimental results are listed in **Table 3.3**.

Table 3.3 Experimental conditions and results

Core Number	Back Pressure (psi)	Temperature (ºF)	Permeability (md)	Porosity	Injection rate (mL/min)	PV_{bt}
1	3000	70	8.19	0.15	1.2	1.43
2	3000	70	8.46	0.15	1.5	0.72
3	3000	70	8.73	0.15	3	0.46
4	3000	70	8.66	0.15	5	0.46
5	3000	70	5.71	0.14	8	0.49
6	3000	70	10.41	0.16	12	0.64
7	2000	70	8.67	0.15	1.2	1.29
8	2000	70	7.28	0.15	1.5	0.59
9	2000	70	9.09	0.15	3	0.44
10	2000	70	9.25	0.16	5	0.38
11	2000	70	8.67	0.15	8	0.53
12	2000	70	7.06	0.16	12	0.51
13	1000	70	7.38	0.15	1.2	0.9
14	1000	70	7.75	0.16	1.5	0.53
15	1000	70	8.19	0.15	3	0.47
16	1000	70	5.73	0.15	5	0.39
17	1000	70	7.63	0.15	6.5	0.39
18	1000	70	6.72	0.15	12	0.58
19	500	70	13.64	0.21	1.5	4.05
20	500	70	5.92	0.1	1.9	1.22
21	500	70	14.55	0.09	3	0.88
22	500	70	10.78	0.14	8	0.48
23	3000	150	12	0.13	1	0.5
24	3000	150	13.79	0.13	3	0.44
25	3000	150	6.13	0.12	5	0.5
26	3000	150	8.08	0.12	5	0.47
27	3000	150	13.43	0.14	8	0.57
28	2000	150	8.73	0.13	1	0.58
29	2000	150	14.24	0.13	3	0.46
30	2000	150	12.06	0.13	5	0.44
31	2000	150	13.43	0.14	8	0.53
32	1000	150	17	0.12	1	4.48
33	1000	150	13.1	0.14	3	0.44

Table 3.3 (Continued)

Core Number	Back Pressure (psi)	Temperature (ºF)	Permeability (md)	Porosity	Injection rate (mL/min)	PV_{bt}
34	1000	150	12.13	0.13	5	0.47
35	1000	150	12.94	0.14	8	0.51
36	500	150	9.7	0.15	2	1.9
37	500	150	10.07	0.13	3	0.76
38	500	150	8.77	0.14	5	0.42
39	500	150	13.18	0.14	8	0.47
40	500	150	14.8	0.15	12	0.6

4. THEORETICAL MODEL AND NUMERICAL SOLUTION

4.1 Introduction

In order to simulate wormhole propagation in two-phase flow region, two problems need to be solved: wormhole propagation and two-phase flow in porous media. The numerical model used in this work for simulating wormhole propagation is an averaged volume continuum model, also called two-scale model. The two-phase flow in porous media part is solved using Implicit Pressure Explicit Saturation (IMPES) method. Brooks and Corey models (Brooks and Corey, 1964) for relative permeability and capillary pressure are implemented. The model is solved numerically by an open-source simulation platform OpenFOAM® (http://www.openfoam.org). An open-source toolbox for multiphase flow (Horgue et al., 2015) is modified and implemented in the model.

The sequence of this section is arranged as follows: first, wormhole propagation model is explained. Then, two-phase flow model is developed, followed by model verification and modification using experimental data from the previous chapter.

4.2 Mathematical model

The dissolution process of carbonate rocks is a combined result of acid transport and pore surface heterogeneous reaction. In order to relate the Darcy scale fluid transport and pore scale acid rock reaction, the averaged continuum model, also called two-scale model is used. In this model, the solid grains are not explicitly described. A cutoff length is introduced, and all the information below this length scale is modeled as a porous medium

(Soulaine and Tchelepi, 2016). The scale corresponds to the domain element for the applicability of Darcy's law. A domain element, which is associated with the cutoff length, contains both solid grain and void space by some proportion characterized by the porosity at that point. The domain element should be large enough that contains solid and void space and the properties can be averaged over the element volume. It should also be small enough that the average properties in each point correctly represents a relatively homogeneous value within the element (Schwalbert et al., 2017). **Fig. 4.1** shows a schematic of different length scales in porous media (Panga, 2003). Porosity ϕ is defined as

$$\phi = \frac{V_{void}}{V} \tag{4-1}$$

where V_{void} is the volume occupied by the void space and V is the volume of the domain element. Each domain element has a given porosity, permeability, velocity, pressure, saturation, and acid concentration. The equations of fluid flow, acid transport, and acid/rock reaction are solved using locally averaged properties. The detailed model development can be found in Panga's work (Panga, 2003; Panga et al., 2005).

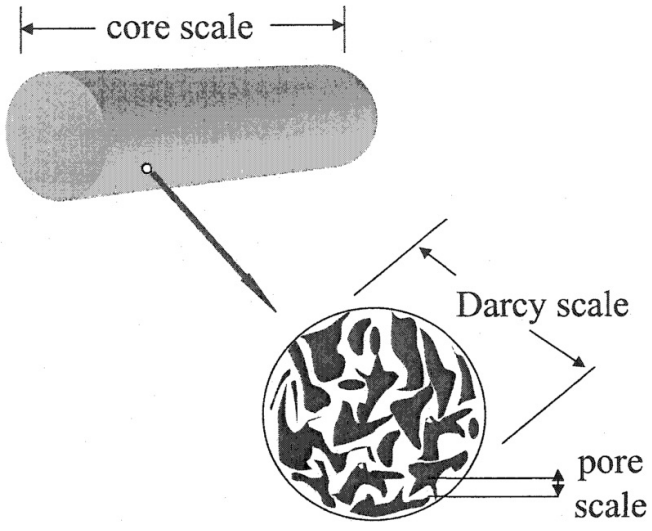

Figure 4.1 Schematic of different scales in a porous medium (Panga, 2003)

In this study, there are three phases present in domain element, a non-wetting phase (gas), a, a wetting phase (acid), b and rock phase, c, as shown in **Fig. 4.2**. Phase a and b are moving phases, rock phase, c can be dissolved during acid injection. Saturation of the moving phase a and b is defined as

$$S_i = \frac{V_i}{V_{void}}, i = a, b \tag{4-2}$$

where V_i is the volume occupied by i-phase in the domain element. As phase a and b are the only moving phases and dissolved rock particles are treated as completely dissolvable, the saturation should satisfy the following relationship:

$$S_a + S_b = 1 \tag{4-3}$$

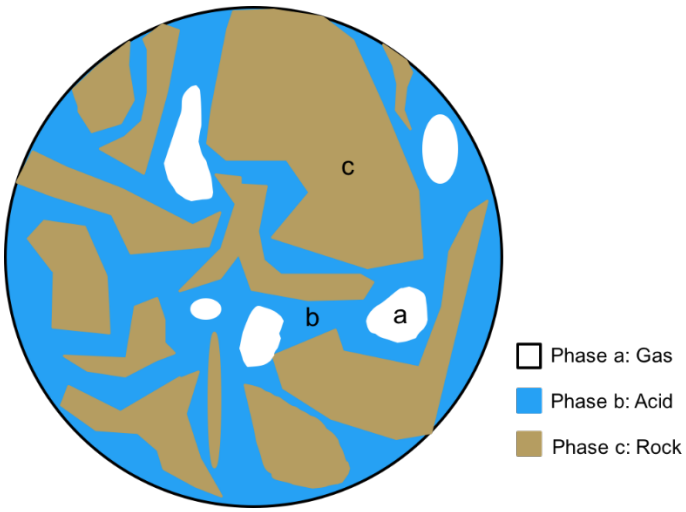

Figure 4.2 Schematic of different phase in system

In wormhole propagation process, the flow in the porous media is governed by the Darcy's Law, while the flow in the wormholes is governed by the Navier-Stokes equation. Darcy-Brinkman-Stokes (Brinkman, 1949) equation can solve this combined problem using one single conservation equation. However, it is shown in the study by Pomès' (2001) study that the Darcy's Law can capture the wormholing behavior and effect of parameters. The Darcy's Law is used in this study instead of Darcy-Brinkman-Stokes equation for computational efficiency.

In this study, acid only exists in the wetting phase. Reservoir rock, wetting phase, and non-wetting phase are constant density. All the rock can react with acid. The reaction process is isothermal.

Considering incompressible two-phase flow in a porous medium, the momentum equation is given by Darcy's Law (Muskat et al., 1937):

$$\boldsymbol{U}_i = -\frac{\boldsymbol{k}_i}{\mu_i} \cdot (\nabla p_i - \rho_i \boldsymbol{g}) \tag{4-4}$$

where $\boldsymbol{U}_i$ is the superficial velocity and $\boldsymbol{k}_i$, μ_i, ρ_i are the rock effective permeability tensor, dynamic viscosity, and density of i-phase, respectively. $\boldsymbol{g}$ is gravitational acceleration.

The effective permeability is defined as

$$\boldsymbol{k}_i = \boldsymbol{K} k_{ri}(S_b) \tag{4-5}$$

where $\boldsymbol{K}$ is the rock absolute permeability tensor for anisotropic reservoirs. The detailed calculation of effective permeability is explained in Section 4.3

The relationship between the pressure of each phase is characterized by

$$p_c(S_b) = p_a - p_b \tag{4-5}$$

where p_c is the capillary pressure and can be measured from laboratory experiments. Experimental data can be correlated using the Brooks and Corey model (Brooks and Corey, 1964), the detailed model is explained in Section 4.4.

Due to the dissolution process, the conservation equation should consider that the porosity varies with time ($\frac{\partial(\phi)}{\partial t} \neq 0$). The mass conservation equation of each phase is given by

$$\frac{\partial(\phi \rho_a S_a)}{\partial t} + \nabla \cdot (\rho_a \boldsymbol{U_a}) = m_a \tag{4-6}$$

$$\frac{\partial(\phi \rho_b S_b)}{\partial t} + \nabla \cdot (\rho_b \boldsymbol{U_b}) = m_b \tag{4-7}$$

where ρ_a and ρ_b are the density of phase a and b. m_b is the mass transfer rate of dissolved mineral. m_a is the a-phase mass generation rate due to acid/mineral reaction. This term is neglected in previous studies in which generated CO_2 is considered dissolved totally in

the liquid phase. However, when considering evolved CO_2 effect during matrix acidizing process in which the generated product present as another phase, it is not negligible.

$$m_a = \rho_a \Gamma_a R(C_s) \tag{4-8}$$

where Γ_a is a stoichiometric coefficient. $R(C_s)$ is the rate of acid consumption due to chemical reaction with the rock, and C_s is the acid concentration at the rock surface. Assuming the dissolved mineral doesn't change the density of the fluid, then

$$S_a \frac{\partial(\phi)}{\partial t} + \phi \frac{\partial(S_a)}{\partial t} + \nabla \cdot (\boldsymbol{U_a}) = m_a/\rho_a \tag{4-9}$$

$$S_b \frac{\partial(\phi)}{\partial t} + \phi \frac{\partial(S_b)}{\partial t} + \nabla \cdot (\boldsymbol{U_b}) = 0 \tag{4-10}$$

Combine Equation 4-3 and 4-4 into 4-8 and 4-9, we get

$$\frac{\partial \phi}{\partial t} - S_b \frac{\partial \phi}{\partial t} - \phi \frac{\partial S_b}{\partial t} + \nabla \cdot \left(-\frac{\boldsymbol{K} k_{ra}(S_b)}{\mu_a} (\nabla p_a - \rho_a \boldsymbol{g}) \right) = m_a \tag{4-11}$$

$$\phi \frac{\partial S_b}{\partial t} + S_b \frac{\partial \phi}{\partial t} + \nabla \cdot \left(-\frac{\boldsymbol{K} k_{rb}(S_b)}{\mu_b} (\nabla p_a - \rho_b \boldsymbol{g} - p_c(S_b)) \right) = 0 \tag{4-12}$$

by summing Equation 4-11 and 4-12, we get

$$\nabla \cdot \left(-\frac{\boldsymbol{K} k_{ra}(S_b)}{\mu_a} (\nabla p_a - \rho_a \boldsymbol{g}) \right) + \nabla \cdot \left(-\frac{\boldsymbol{K} k_{rb}(S_b)}{\mu_b} (\nabla p_a - \rho_a \boldsymbol{g} - p_c(S_b)) \right) + \frac{\partial \phi}{\partial t} = m_a \tag{4-13}$$

Acid concentration in the wetting phase is solved by acid chemical species balance equation, expressed as:

$$\frac{\partial(\phi S_b C_b)}{\partial t} + \nabla \cdot (\boldsymbol{U_b} C_b) - \nabla \cdot \left(\phi S_b D_{eff} \nabla C_b \right) = -a_{vw} R(C_s) \tag{4-14}$$

where S_b is b phase saturation, C_b is average acid concentration in wetting phase, D_{eff} is effective diffusivity coefficient of the acid. $R(C_s)$ is the rate of acid consumption due to chemical reaction with the rock, and C_s is the concentration at the rock surface. In this

equation, the acid concentration is mass fraction of acid, for 15% acid, C_b is 0.15. a_{vw} is the solid rock specific surface area in the unit area of fluid-rock contact per volume of porous medium contacting with the wetting phase, where a_{vw} can be defined as (El-Amin et al., 2015):

$$a_{vw} = a_{vw}(S_w, p_c) = \alpha_1 S_w (1 - S_w)^{\alpha_2} p_c^{\alpha_3} \tag{4-15}$$

where $\alpha_1, \alpha_2, \alpha_3$ are constants.

As gas is inert to rock and acid fluid, instead of the above complicated formula, we assume the acid/rock contacting specific area depends only on wetting phase saturation, as

$$a_{vw} = a_v S_b \tag{4-16}$$

In this work, the reaction between hydrochloric acid and limestone is considered as irreversible first order kinetics as used in most previous literature (Panga et al., 2005; Kalia, 2008; De Oliveira et al., 2012; Maheshwari et al., 2013). The reaction rate is given by

$$R(C_s) = k_s C_s \tag{4-17}$$

where k_s is surface reaction rate constant with unit same as velocity.

The chemical reaction between acid and rock involves three processes: acid transport to rock surface, acid reaction with rock, reaction product transport away from rock surface. As the reaction rate between HCl and $CaCO_3$ is much higher than acid transportation rate, acid flux transported to the acid/rock contact is consumed instantaneously. Acid flux transport to the rock surface is

$$J_{acid} = k_c (C_b - C_s) \tag{4-18}$$

where J_{acid} is acid flux, k_c is acid mass transfer coefficient. By equating Equation 4-17 and 4-18, we get

$$k_c(C_b - C_s) = k_s C_s \tag{4-19}$$

then,

$$C_s = \frac{k_c}{k_s + k_c} C_b \tag{4-20}$$

substituting Equation 4-16, 4-17, 4-20 into 4-14, we can get

$$\frac{\partial(\phi S_b C_b)}{\partial t} + \nabla \cdot (\boldsymbol{U_b} C_b) - \nabla \cdot \left(\phi S_b D_{eff} \nabla C_b\right) = a_v S_b \left(\frac{k_s k_c}{k_s + k_c}\right) C_b \tag{4-21}$$

Here, we define effective mass transfer coefficient as

$$k_{eff} = \left(\frac{k_s k_c}{k_s + k_c}\right) \tag{4-22}$$

For mass transfer dominated process, $k_s \gg k_c$, and $k_{eff} \approx k_c$. For reaction dominated process, $k_c \gg k_s$, and $k_{eff} \approx k_s$. As wormhole propagates, the porosity field is updated based on the acid/rock reaction. The consumed acid amount is related to the mass of dissolved rock by:

$$\frac{\partial \phi}{\partial t} = a_v S_b \left(\frac{k_s k_c}{k_s + k_c}\right) C_b \beta_{100} \frac{\rho_b}{\rho_c} \tag{4-23}$$

where β_{100} is gravimetric dissolving power for HCl, ρ_c is rock density in kg/m^3.

Equation 4-10, 4-13, 4-21 and 4-23 are the main equations for wormhole propagation model, which can be solved for saturation, pressure, acid concentration, and porosity evolution.

4.3 Relative permeability model

In this study, Brooks and Corey relative permeability model (Brooks and Corey, 1964) is used. Typical relative permeability cure is shown in **Fig. 4.3**. For each simulation, the relative permeability data are collected from the previous study and curve fitted using this model.

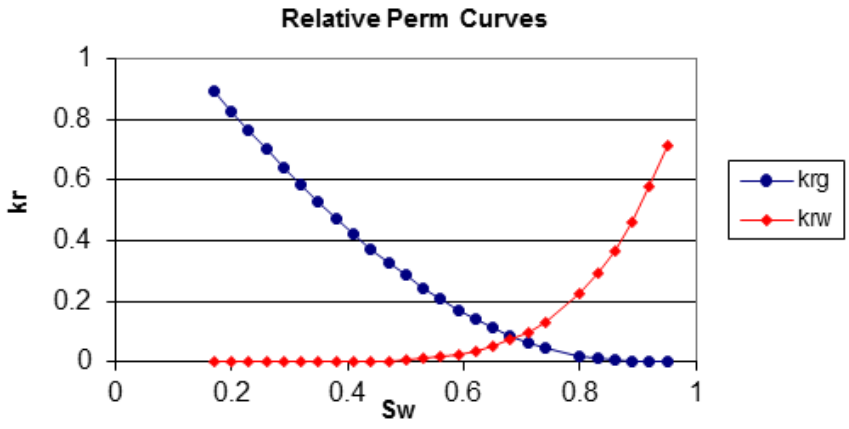

Figure 4.3 Example of relative permeability curve

Brooks and Corey model define effective saturation $S_{b,eff}$ as

$$S_{b,eff} = \frac{S_b - S_{b,irr}}{1 - S_{b,irr}} \tag{4-24}$$

where $S_{b,irr}$ is the irreducible wetting phase saturation. The relative permeability of each phase is defined as

$$k_{ra}(S_{b,eff}) = k_{ramax}(1 - S_{b,eff})^{m_n} \tag{4-25}$$

$$k_{rb}(S_{b,eff}) = k_{rbmax} S_{b,eff}^{m_w} \tag{4-26}$$

where k_{ramax} and k_{rbmax} are the endpoint relative permeability for non-wetting phase and wetting phase. m_n and m_w are the power coefficient for each phase.

4.4 Capillary pressure model

Brooks and Corey capillary model (Brooks and Corey, 1964) is also used in this study. **Fig. 4.4** shows a typical capillary pressure curve get from experimental data.

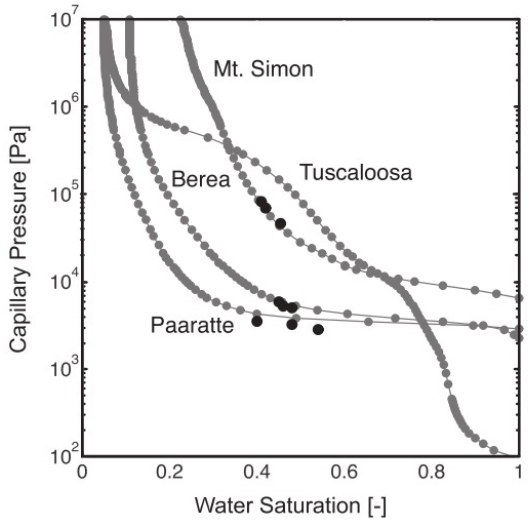

Figure 4.4 Example of capillary pressure date from experiment (Krevor et al., 2012)

In Brooks and Corey model, the capillary pressure correlation is based on effective saturation, and is calculated as

$$p_c(S_b) = p_{c,0} S_{b,eff}^{1/\alpha} \tag{4-27}$$

where $p_{c,0}$ is the entry capillary pressure and α is pore size distribution index.

4.5 Mass transfer and diffusion coefficient

Acid mass transfer coefficient, k_c, is a rate constant that describes the acid mass transfer rate from bulk acid to rock surface. As mentioned before, the relative ratio of k_c and the surface reaction rate constant, k_s, determines whether the reaction is mass-transfer limited or reaction rate limited.

For the mass transfer coefficient, k_c, the correlation used by most previous studies (Panga et al., 2003; Kalia, 2008; Soulaine and Tchelepi, 2016; Schwalbert et al., 2017) is related to Sherwood number, Sh, pore scale Reynolds number, Re_p, and Schmidt number, S_c, these parameters are defined as

$$Sh = \frac{2k_c r_p}{D_m} \tag{4-28}$$

$$Re_p = \frac{2r_p \rho_b |U_b|}{\mu_b} \tag{4-29}$$

$$Sc = \frac{\mu_b}{\rho_b D_m} \tag{4-30}$$

$$Sh = Sh_\infty + bRe_p^{1/2} Sc^{1/3} \tag{4-31}$$

Where r_p is the pore radius, Sh_∞ is the asymptotic Sherwood number. The typical value for Sh_∞ is 3.66 for circular cross-section, and is adopted in this work. b is related to pore length to diameter ratio, and is 0.7 in this work, the same as that used in the work of Maheshwari and Balakotaiah (2013). Fluid flows through porous media are often characterized by a pore scale Reynolds number Re_p (Hall and Hiatt, 1996). As in this study, there are two phases flow in pore area, mixture velocity, density, and viscosity should be used. However, for the simplicity of calculation, wetting phase properties are used in pore scale Reynolds number and Schmidt number equation.

In porous media, solution diffusion is hindered by the tortuous nature of the pores, the diminished cross-sectional area and possibly by the pore sizes (Grathwohl, 1998). Under water-saturated conditions, the effective diffusivity, D_{eff}, is defined as

$$D_{eff} = (D_m \phi_e \delta)/\tau_f \tag{4-32}$$

where τ_f and δ are dimensionless factors accounting for tortuosity (>1) and constrictivity (≤ 1) of the pores, respectively. ϕ_e is the effective transport-through porosity. D_m is the effective molecular diffusivity of the acid.

When only overall porosity is known, the effective diffusivity is defined as an empirical function of ϕ, and

$$D_{eff} = \phi^m D_m \tag{4-33}$$

where m is an empirical exponent.

In this study, for simplification, $m = 1$ is used, and

$$D_{eff} = \phi D_m \tag{4-34}$$

4.6 Pore scale model

During the acidizing process, porosity increases with time and changes pore structure. A pore scale model relating parameters r_p, a_v, $\boldsymbol{K}$ to local porosity is needed.

Kozeny-Carman equation is commonly used for porosity-permeability correlation. Due to different properties of rock, several correlations have been developed. Civan (2000) reviewed different models relating permeability to porosity for carbonates. He developed a permeability-porosity correlation called power-law flow units equation, as follows:

$$\frac{K}{K_0} = f_\infty \frac{\phi}{\phi_0} \left[\frac{\phi(1-\phi_0)}{\phi_0(1-\phi)}\right]^{2\beta} \tag{4-35}$$

where ϕ_0 and K_0 are initial permeability of the rock. f_∞ and β are empirical numbers from curve fitting. **Fig. 4.5** is an example of permeability-porosity relationship of different rock correlated using the Civan's equation.

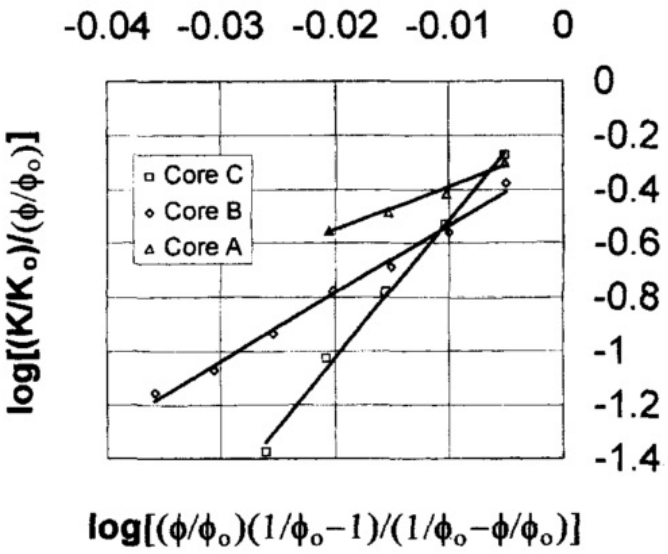

Figure 4.5 Straight-line plots of permeability vs. porosity by Civan equation (Civan, 2000)

Due to the heterogeneous of carbonates, it is difficult to relate permeability to porosity in a single correlation. The relationship between permeability and porosity may also change during the dissolution process. Ziauddin and Bize (2007) collected the evolving porosity and permeability data for several different rocks, as shown in **Fig. 4.6**. The relationships were obtained by injecting 0.5M HEDTA into different rock samples at

15 mL/min. **Fig. 4.6** suggests that the permeability-porosity relationship is non-linear and is related to different rock types.

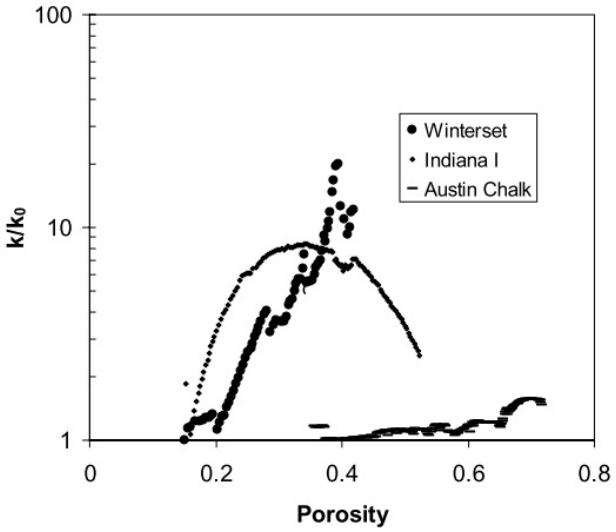

Figure 4.6 Evolution of permeability with porosity (Ziauddin and Bize, 2007)

In this study, in order to simulate the permeability evolution, we adopt the following permeability porosity relationship as used in previous studies (Kalia and Balakotaiah, 2007; Maheshwari et al., 2013):

$$\frac{K}{K_0} = \frac{\phi}{\phi_0}\left[\frac{\phi(1-\phi_0)}{\phi_0(1-\phi)}\right]^{2\beta} \tag{4-36}$$

the parameter β is introduced to account for rock dissolution and may be different for each rock type.

The other correlations used in this study are as follows (Schwalbert et al., 2017):

$$\frac{r_p}{r_{p0}} = \left(\frac{\phi}{\phi_0}\right)^{\gamma} \tag{4-37}$$

$$\frac{a_v}{a_{v0}} = \left[\left(\frac{\phi_0}{\phi}\right)\left(\frac{1-\phi}{1-\phi_0}\right)\right]^{\eta} \tag{4-38}$$

where r_{p0} and a_{v0} are the initial pore radius and initial specific surface area. γ and η are adjustable parameter. As $\phi \to 1$, $a_v \to 0$, which causes the reaction rate to be zero. Note that the initial permeability $\boldsymbol{K_0}$ may not be related to initial porosity, ϕ_0.

4.7 Model implementation

In this work, the complex system is solved numerically using the finite volume method in an open source computational fluid dynamics software Open Source Field Operation and Manipulation (OpenFOAM®). The OpenFOAM® software handles complex three-dimensional grids and has demonstrated good scalability for parallel computation of flow in porous media (Soulaine and Tchelepi, 2016). The mathematical model described is non-linear due to relative permeability and capillary pressure. In order to solve this system, Implicit Pressure Explicit Saturation (IMPES) method is used. The IMPES algorithm was first introduced by Sheldon et al. (Sheldon et al., 1959). The IMPES method takes all variables explicit, except for pressure, resulting in significant computational effort reduction. The "anisoImpesFoam" solver from "an open-source tool box for multiphase flow in porous media (Horgue et al., 2015)" is modified and implemented.

In order to implement the model, the following formulations are used.

First, we define the phase mobility M_i, and gravitational contribution L_i, as follows:

$$M_i = \frac{Kk_{ri}(S_b)}{\mu_i} \tag{4-39}$$

$$L_i = \frac{Kk_{ri}(S_b)}{\mu_i}\rho_i \tag{4-40}$$

Assuming that capillary pressure is only related to saturation, then we have

$$\nabla p_c = \frac{\partial p_c}{\partial S_b} \nabla S_b \tag{4-41}$$

Thus, Equation 4-10 and 4-13 can be expressed as

$$-\nabla \cdot ((M_a + M_b)\nabla p_a + \nabla \cdot \left((L_a + L_b)g + M_b \frac{\partial p_c}{\partial S_b} \nabla S_b \right) + \frac{\partial \phi}{\partial t} = 0 \tag{4-42}$$

$$\frac{\partial (\phi S_b)}{\partial t} + \nabla \cdot \left(-M_b \nabla p_a + L_b g + M_b \frac{\partial p_c}{\partial S_b} \nabla S_b \right) = 0 \tag{4-43}$$

Here, we define three fluxes: pressure gradient flux, gravity flux and capillary pressure flux. These fluxes are defined at each face of the computational grid block.

$$\Phi_p = \left(M_{a,c\to f} + M_{b,c\to f} \right) \nabla p_a \cdot \boldsymbol{S}_f \tag{4-44}$$

$$\Phi_g = \left(L_{a,c\to f} + L_{b,c\to f} \right) \mathbf{g} \cdot \boldsymbol{S}_f \tag{4-45}$$

$$\Phi_{pc} = M_{b,c\to f} \left(\frac{\partial p_c}{\partial S_b} \nabla S_b \right)_{c\to f} \cdot \boldsymbol{S}_f \tag{4-46}$$

where $c \to f$ refers that the cell center values are interpreted to a face-centered value. In order to calculate these values, the related parameters such as permeability and viscosity should also be interpreted to face-centered value.

From the above equations, the global flux can be calculated as

$$\Phi = \Phi_p + \Phi_g + \Phi_{pc} \tag{4-47}$$

And the flux of phase b can be calculated as

$$\Phi_b = \frac{M_{b,c\to f}}{M_{a,c\to f} + M_{b,c\to f}} \Phi_p + \frac{L_{b,c\to f}}{L_{a,c\to f} + L_{b,c\to f}} \Phi_g + \Phi_{pc} \tag{4-48}$$

and the flux of phase a can be calculated as

$$\Phi_a = \Phi - \Phi_b \tag{4-49}$$

Note that in this process, global flux Φ is conservative, and flux of each phase is calculated.

Then, Equation 4-42 and 4-43 are turned into

$$\nabla \cdot \left(M_{a,c\to f} + M_{b,c\to f}\right)\nabla p_a - \nabla \cdot \Phi_g - \nabla \cdot \Phi_{pc} + \frac{\partial \phi}{\partial t} = 0 \tag{4-50}$$

$$\frac{\partial(\phi S_b)}{\partial t} + \nabla \cdot \Phi_b = 0 \tag{4-51}$$

the above two equations are implemented into the solver.

Acid chemical species balance equation (Equation 4-21) need to be solved implicitly. During the discretizing process, we need to ensure C_f is positive. The source term ($a_v S_b \left(\frac{k_s k_c}{k_s + k_c}\right) C_b$) needs to be modified, as it is solution dependent. The source term is linearized in terms of the dependent variable and split into two parts, one treated explicitly and the second treated implicitly (F. Moukalled, L. Mangani, 2016), as follows

$$S(\varphi) = S_p \varphi + S_u \tag{4-52}$$

where S_p is the implicit part and S_u is the explicit part. In order to keep C_f positive, $S_p < 0$, and $S_u > 0$, are required. Thus,

$$S_p = -a_v S_b \rho_b \left(\frac{k_s k_c}{k_s + k_c}\right) C_b \tag{4-53}$$

$$S_u = 0 \tag{4-54}$$

The porosity evolution equation (Equation 4-23) also has variable dependent source term ($a_v S_b \left(\frac{k_s k_c}{k_s + k_c}\right) C_b \beta_{15} \frac{\rho_b}{\rho_c}$). In order to keep porosity ϕ in the range of [0,1], the source term is defined as

$$S(\varphi) = A\phi(1 - \phi) \tag{4-55}$$

where $S(\varphi) > 0$, when $A > 0$, ϕ increases; when $\phi > 1$, we got $S(\varphi) < 0$, then ϕ decrease back into the range of [0,1]. According to Equation 4-54, we have

$$S(\varphi) = [-A\phi\,]\phi + [A\phi] \tag{4-56}$$

As the source term is

$$S(\varphi) = a_{v0}\left[\left(\frac{\phi}{\phi_o}\right)\left(\frac{1-\phi}{1-\phi_0}\right)\right]^{\eta} S_b\left(\frac{k_s k_c}{k_s+k_c}\right) C_b \beta_{15} \frac{\rho_b}{\rho_c} \tag{4-57}$$

We got

$$A = \frac{a_{vo}\left[\left(\frac{\phi}{\phi_o}\right)\left(\frac{1-\phi}{1-\phi_o}\right)\right]^{\eta} S_b\left(\frac{k_s k_c}{k_s+k_c}\right) C_f \beta \frac{\rho_b}{\rho_{rock}}}{\phi(1-\phi)} \tag{4-58}$$

$$S_p = -\frac{a_{vo}\left[\left(\frac{\phi}{\phi_o}\right)\left(\frac{1-\phi}{1-\phi_0}\right)\right]^{\eta} S_b\left(\frac{k_s k_c}{k_s+k_c}\right) C_f \beta \frac{\rho_b}{\rho_{rock}}}{(1-\phi)} \tag{4-59}$$

$$S_u = \frac{a_{vo}\left[\left(\frac{\phi}{\phi_o}\right)\left(\frac{1-\phi}{1-\phi_o}\right)\right]^{\eta} S_b\left(\frac{k_s k_c}{k_s+k_c}\right) C_f \beta \frac{\rho_b}{\rho_{rock}}}{(1-\phi)} \tag{4-60}$$

The mass transfer coefficient k_c, the pore radius r_p, and the specific surface area a_v are all heterogeneous and vary with time, and should be updated each time step as porosity evolution.

4.8 Boundary and initial conditions

4.8.1 Boundary conditions

A constant injection velocity is imposed at the inlet of the domain, which is the common condition when doing matrix acidizing experiments. The outlet pressure is a fixed value. As we are using a constant injection rate, the pressure is just the differential pressure across the core, we can set the fixed value at outlet as 0.

"Darcy velocity" boundary condition developed by Horgue (2015) is adopted. Assuming fixed phase velocities on the considered boundary, the total velocity can be expressed

$$\boldsymbol{U}_{fixed} = \boldsymbol{U}_{a,fixed} + \boldsymbol{U}_{b,fixed}$$

$$= -\nabla \cdot ((M_a + M_b)\nabla p_a + \nabla \cdot \left((L_a + L_b)\boldsymbol{g} - M_b \frac{\partial p_c}{\partial S_b} \nabla S_b \right) \tag{4-61}$$

then, the Neumann boundary condition is

$$\boldsymbol{n} \cdot \nabla p_a = \boldsymbol{n} \cdot \left[(M_a + M_b)^{-1} \left(\boldsymbol{U}_{fixed} - (L_a + L_b)\boldsymbol{g} + M_b \frac{\partial p_c}{\partial S_b} \nabla S_b \right) \right] \tag{4-62}$$

where $\boldsymbol{n}$ is the normal to the face boundary. This boundary condition is called "darcyGradPressure" in the solver.

4.8.2 Initial conditions

At the beginning of the simulation, the initial porosity, permeability, pore radius, and specific surface area should be defined. In order to create wormholes, local heterogeneity is needed.

In previous studies (Panga et al., 2005; Kalia and Balakotaiah, 2007; Liu et al., 2012; Schwalbert et al., 2017), uniform, normal, and lognormal distribution have been used to generate permeability and porosity fields. Zakaria et al. (2015) and Dubetz et al. (2016) used micro-CT scan and NMR method to collect the pore size distribution of several carbonate rock samples commonly used in experimental study. From their results, a lognormal distribution may be a more precise way to populate both porosity and permeability fields. **Figure. 4.7** shows the pore size distribution following lognormal

distribution. In this study, lognormal distribution is used for porosity and permeability field generation. To generate the porosity and permeability field, the following equations are used

$$\phi = e^{\left[\ln(\phi_{mean}) - \frac{\sigma_\phi^2}{2} + \sigma_\phi Z_n\right]} \tag{4-63}$$

$$\boldsymbol{K} = e^{\left[\ln(\overline{k_{\max}}) - \frac{\sigma_k^2}{2} + \sigma_k Z_n\right]} \left(\frac{1}{\overline{k_{max}}}\right) \overline{\boldsymbol{K}} \tag{4-64}$$

where Z_n is a standard normally distributed random number, generated using OpenFOAM's function *GaussNormal()*. ϕ_{mean} and σ_ϕ are the mean and standard deviation of natural logarithm of porosity values. $\overline{\boldsymbol{K}}$ is permeability tensor, and is constructed as

$$\overline{\boldsymbol{K}} = \begin{bmatrix} \overline{k_H} & 0 & 0 \\ 0 & \overline{k_V} & 0 \\ 0 & 0 & \overline{k_Z} \end{bmatrix} \tag{4-65}$$

where $\overline{k_H}$, $\overline{k_V}$, $\overline{k_Z}$ are the mean permeability in horizontal, vertical, and z-direction. $\overline{k_{max}}$ is the maximum value of the above three permeability values.

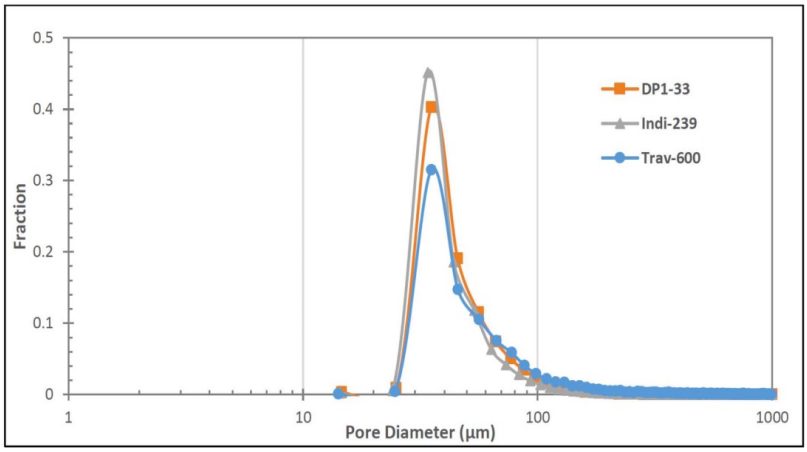

Figure 4.7 Pore size distribution in lognormal distribution (Dubetz et al., 2016)

4.9 Algorithm

The equations are solved in OpenFOAM® as the following steps.

1. All the properties related to porosity are updated, such as relative permeability, rock pore radius, etc.
2. The saturation equation is solved explicitly using the last time Φ_b

$$\frac{\phi^n S_b^{n+1} - \phi^n S_b^n}{\Delta t_{n+1}} + \nabla \cdot \Phi_b^n = 0 \tag{4-66}$$

3. Properties related to saturation are updated, such as $M_a^{n+1}, M_b^{n+1}, L_a^{n+1}, L_b^{n+1}, \left(\frac{\partial p_c}{\partial S_b} \nabla S_b\right)^{n+1}$ and related fluxes.
4. Pressure field p^{n+1} is solved implicitly by solving the pressure equation

$$\nabla \cdot \left(M_{a,c\to f}^{n+1} + M_{b,c\to f}^{n+1}\right) \nabla p_a^{n+1} - \nabla \cdot \Phi_g^{n+1} - \nabla \cdot \Phi_{pc}^{n+1} + \frac{\phi^n - \phi^{n-1}}{\Delta t_{n+1}} = 0 \tag{4-67}$$

5. The acid concentration equation is solved implicitly
6. The porosity evolution equation is solved

7. Check if acid breakthrough the core, if not, proceed to the next step.

The flow chart of the algorithm is shown in **Fig. 4.8.**

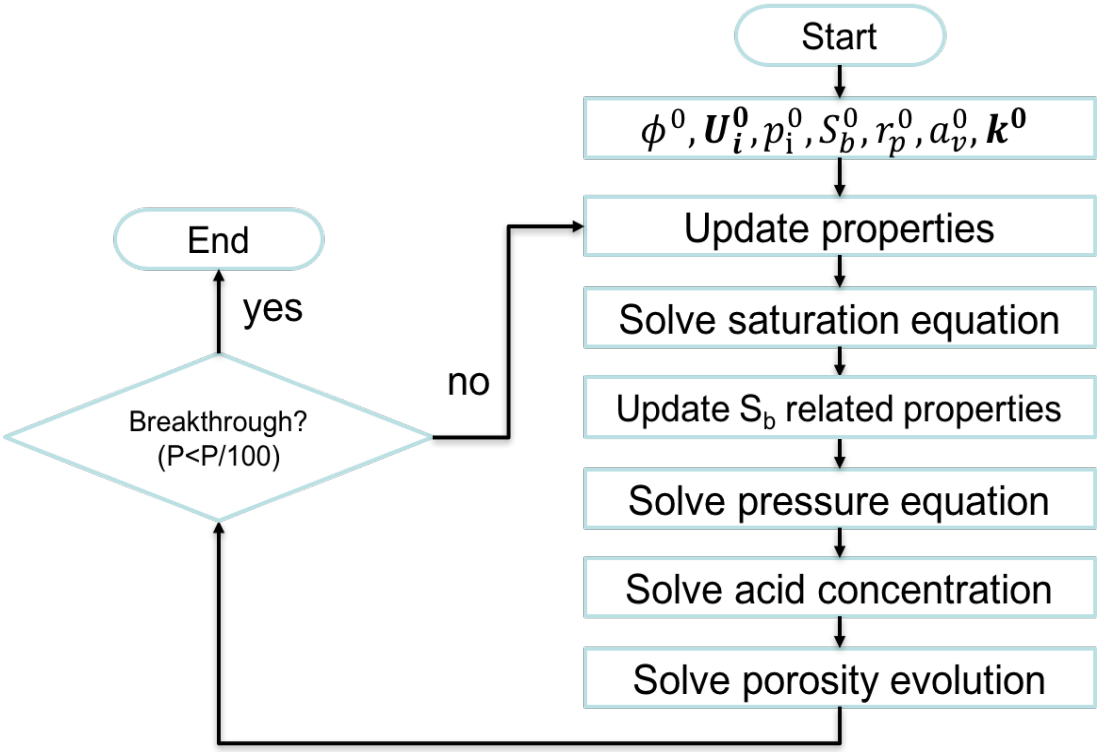

Figure 4.8 Algorithm flowchart

4.10 Solver structure

The overall structure of OpenFOAM® is shown in **Fig. 4.9**. OpenFOAM is supplied with pre- and post-processing environments.

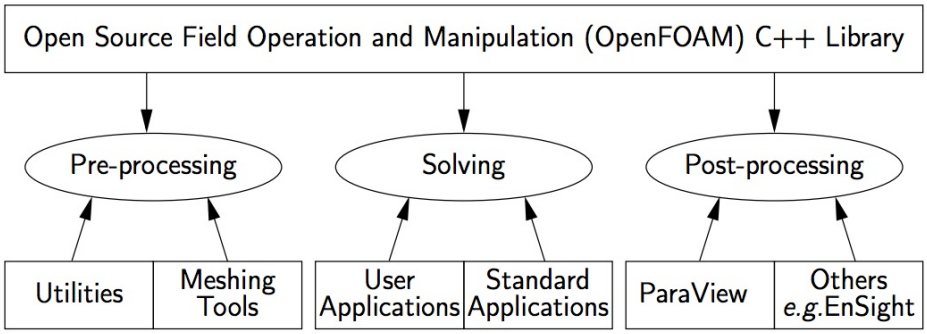

Figure 4.9 OpenFOAM structure

Our solver *wormhole2PhFoam* is implemented as user application into OpenFOAM environment. The structure of *womhole2PhFoam* solver is shown in **Fig. 4.10**. The program consists of three parts: solver, libraries, and example. Solver folder contains the files needed for compiling the solver, Libraries folder contains the models for boundary condition calculation, capillary pressure calculation and relative permeability calculation. Examples folder contains the problems we need to solve.

In Examples folder, there are three subfolders: 0, constant and system. The 0 folder contains all the initial condition of the problem. The constant folder is used for gravitational acceleration, transport properties (phase properties, relative permeability model parameter, transport coefficients). And the System folder contains mesh information, control parameter for the solver, numerical schemes settings.

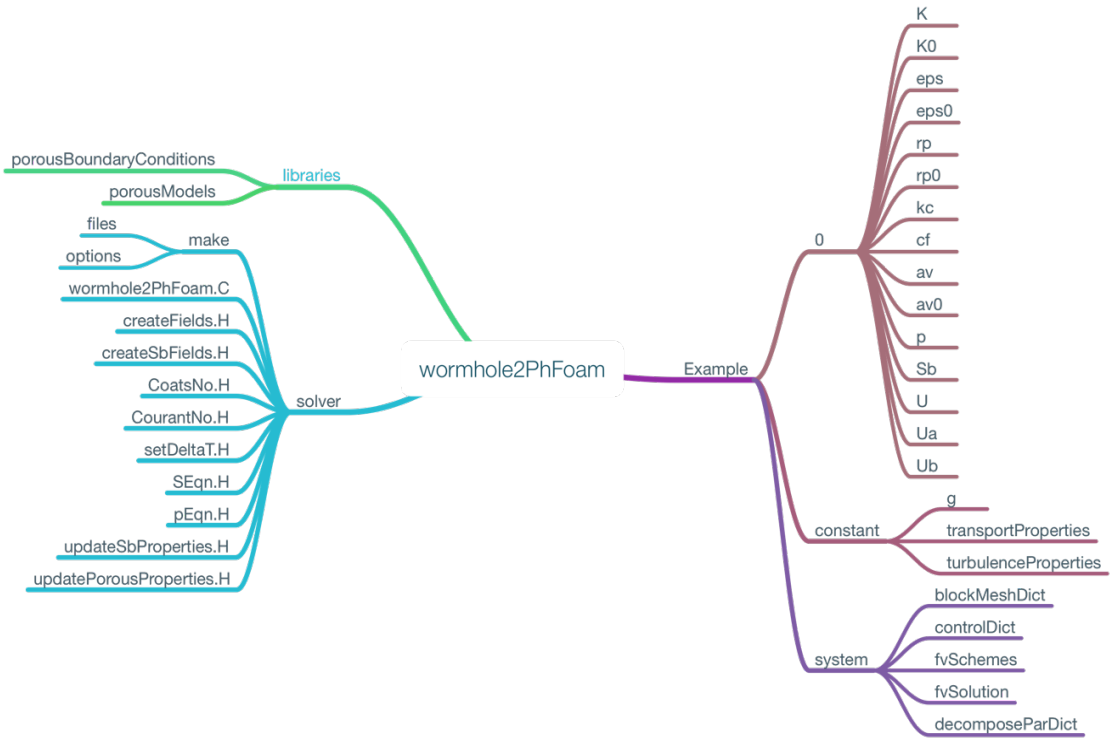

Figure 4.10 Structure of *wormhole2PhFoam*

4.11 Model validation

4.11.1 Single-phase model validation

In order to validate the model and tune the parameters, we need to match experimental data. The detailed validation of capillary pressure model can be found in Horgue's work (Horgue et al., 2015). Here, we first validate the model with single-phase matrix acidizing experimental results. As the model is used to investigate two-phase flow effect, the experimental data present in previous experiments is chosen. The simulation case is matrix acidizing core flooding experiments of Indiana limestone with 15 wt% HCl at 150ºF, 3000 psi.

The simulation domain used in this study is a 3-D block, as shown in **Fig. 4.11**. The cross-sectional area of the simulation domain is equal to that of a 1.5-inch diameter core (3.38 cm ×3.38 cm). The length of the domain is 8 inches. The domain contains 55296 computation cells with a 96 × 24 × 24 mesh. The initial permeability and porosity are lognormal distributed, as shown in **Fig. 4.12** and **4.13**.

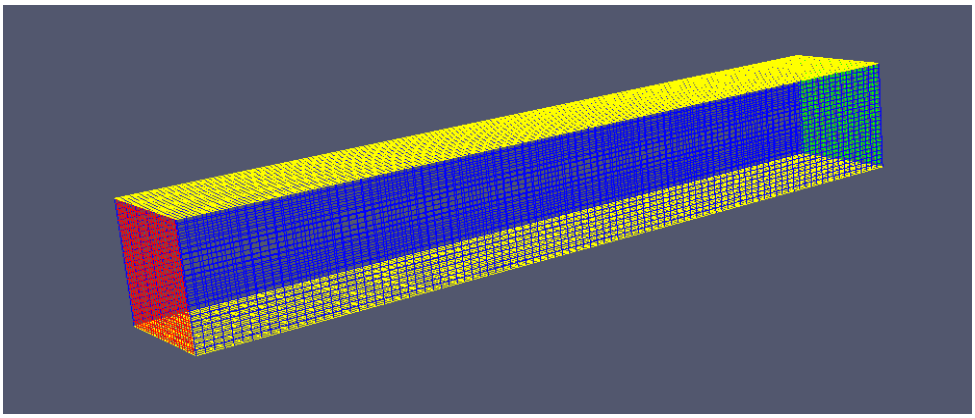

Figure 4.11 Example of simulation domain

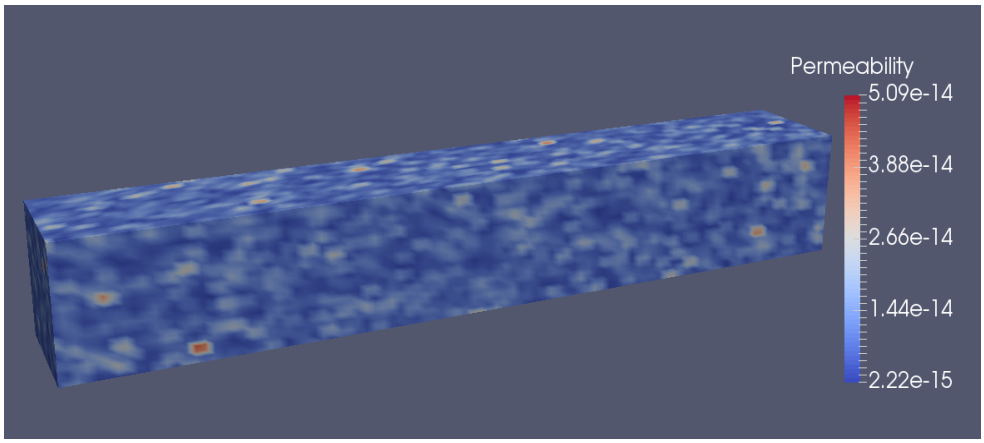

Figure 4.12 Lognormal distribution initial permeability field (m^2)

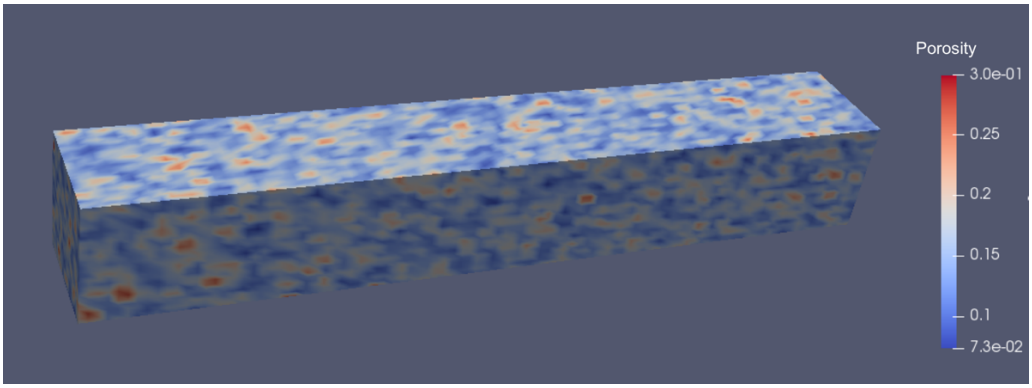

Figure 4.13 Lognormal distribution initial porosity field

The parameters used in the simulation are listed in **Table 4.1**. The core is initially filled with water which has the same density and viscosity as acid fluid. The injected fluid is acid with wetting phase saturation, $S_b = 1$. Capillary pressure term and gravity term are turned off for this simulation. The acid molecular diffusivity and reaction rate constant are obtained from previous studies (Mumallah 1991; de Rozieres 1994; Mumallah 1996;).

Table 4.1 Parameters for single-phase validation

Parameters	**Symbol**	**Units**	**Value**
Core length	-	inch	8
Core diameter	-	inch	1.5
Initial rock mean porosity	ϕ_0	-	0.15
Parameter of lognormal porosity distribution	σ_ϕ	-	0.4
Initial rock mean horizontal permeability	$\overline{k_H}$	md	8
Initial rock mean vertical permeability	$\overline{k_V}$	md	8
Parameter of lognormal permeability distribution	σ_k	-	0.8
Initial rock mean specific surface area	$\overline{a_{v0}}$	m^{-1}	500
Mean initial pore radius	$\overline{r_{p0}}$	m	10^{-5}
Acid Density	ρ_b	kg/m^3	1040
Acid Dynamic viscosity	μ_b	cp	1
Initial Saturation	S_b	-	1
Inlet Acid Saturation	S_b	-	1
Acid molecular diffusivity	D_m	m^2/s	3.6×10^{-9}
Surface reaction-rate constant	k_s	m/s	0.015
Acid gravimetric dissolving power	β_{100}		1.37
Rock Mineral Density	ρ_m	kg/m^3	2710
Pore radius evolution parameter	γ	-	8
surface area evolution parameter	η	-	0.33
Permeability evolution parameter	δ	-	3

The simulation results are shown in **Fig. 4.14**. The blue dots are experimental results, and the orange curve are data fitted using Buijse and Glasbergen Model. The green square are the simulated results. Note that the parameter γ, η, δ are three tuning factors of

the system. Tuning these parameters can change the simulation results. And they should be regarded as the properties related to the core samples and should be tuned for different rock.

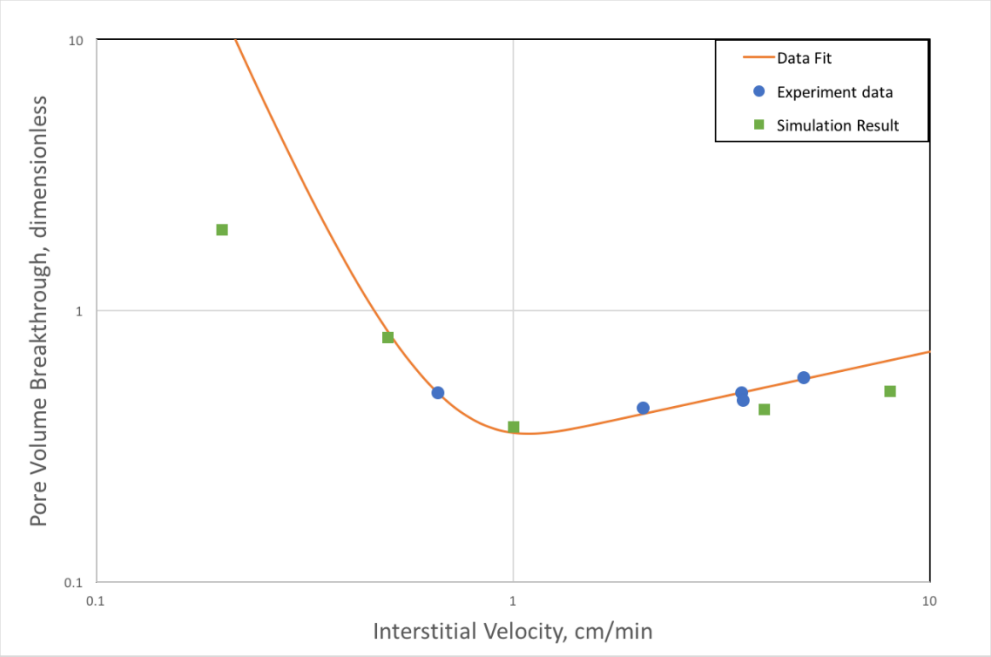

Figure 4.14 Simulation results matching with experimental data (Cheng et al., 2016)

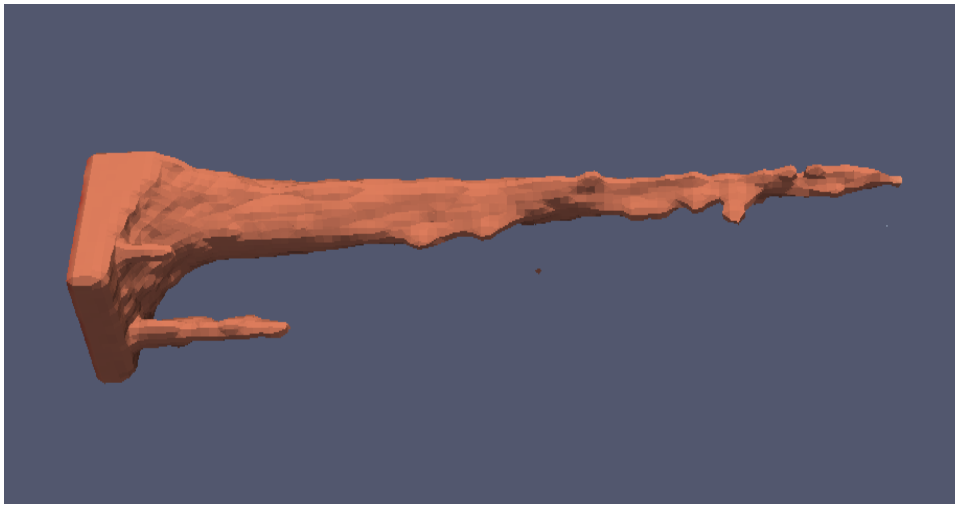

Figure 4.15 Injection flux U = 0.4 cm/min, conical wormhole

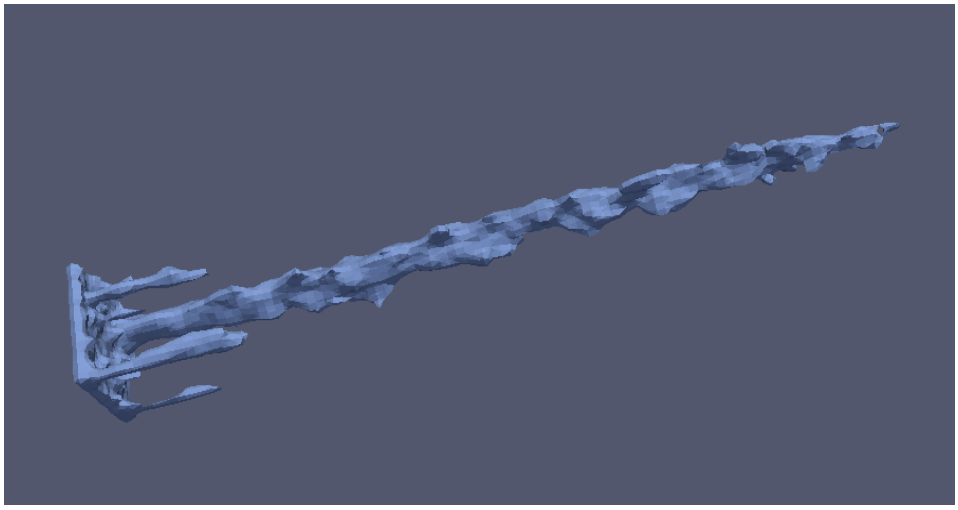

Figure 4.16 Injection flux U = 1 cm/min, dominant wormhole

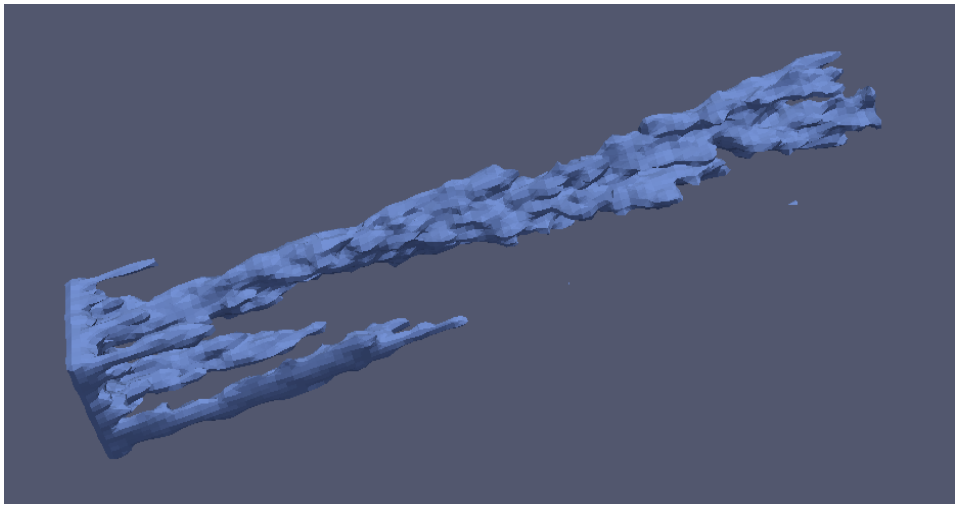

Figure 4.17 Injection flux U = 20 cm/min, ramified wormhole

Fig. 4.15 to **4.17** show simulation results of different wormhole patterns under different injection rate. For injection rate lower than optimal condition (U = 0.4 cm/min), conical wormhole pattern is generated. At optimal condition (U = 1 cm/min), a dominant wormhole with little branches is formed. At high injection rate (U = 20 cm/min), a ramified wormhole is formed with a lot of branches. The plotted figures are the volume of porosity from 0.4 to 1.

From the above results, we can see that the simulator can be used as a single-phase wormhole propagation model and match the experimental data very well. The parameters tuned from this simulation are used in next chapter for two-phase matrix acidizing investigation.

4.11.2 Two-phase model validation

Alternating gas/acid injection was reported in Shukla's work (Shukla et al., 2003) with nitrogen and acid injection alternatively. From the result, it showed the breakthrough pore volume needed for alternating injection of gas and acid (**Fig. 4.18c**) is higher than only acid injection (**Fig. 4.18a**) and the one with gas preconditioning required least amount of acid (**Fig. 4.18b**). The wormhole from alternating injection (**Fig. 4.18c**) showed more branches and larger wormhole diameter. In his work, he also studied acid injection into oil saturated cores, as shown in **Fig. 4.19**. The breakthrough pore volume for oil saturated core is less than gas saturated core. Three conditions are simulated in this study: acid injection to water saturated core, acid injection with alternating nitrogen and acid, acid injection into oil saturated core.

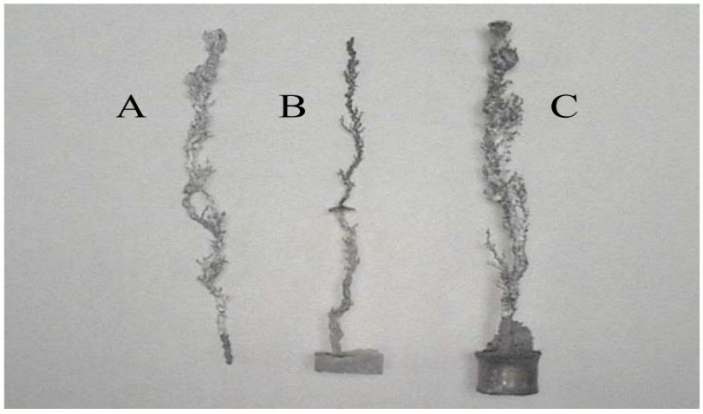

Figure 4.18 Wormhole casting: (A) without gas injection, (B) with gas preconditioning, (C) Alternating gas and acid injection (Shukla et al., 2003)

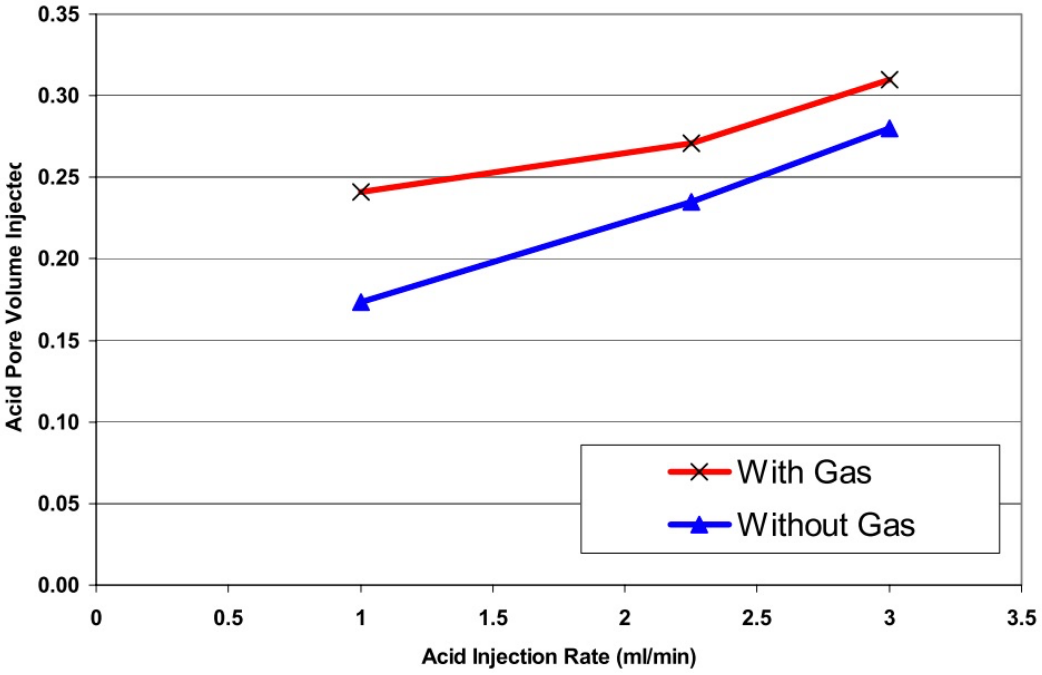

Figure 4.19 Oil saturated cores with and without gas injection (Shukla et al., 2003)

A 3-D domain is constructed for this simulation using the same dimensions as mentioned in Section 4.11.1, as shown in **Fig. 4.11-4.13**. The simulator is tuned using the experimental data of acid injection into water saturated cores in Shukla's work (2003). During the tuning process, capillary pressure term, the mass rate of generated CO_2 and gravity term are set to zero. Parameters for simulating this problem are listed in **Table 4.2**. When simulating alternating gas/acid injection and acid injection into oil saturated core, capillary pressure term is turned on. The experimental data for relative permeability and capillary pressure for nitrogen and water are shown in **Fig. 4.20** (Li and Horne, 2003). Parameters used in Brooks and Corey's model are obtained by curve fitting the experimental data. Other parameters related to two-phase flow are listed in **Table 4.3.**

Table 4.2 Parameters for two-phase validation

Parameters	**Symbol**	**Units**	**Value**
Core length	-	inch	6
Core diameter	-	inch	1
Initial rock mean porosity	ϕ_0	-	0.28
Parameter of lognormal porosity distribution	σ_ϕ	-	0.4
Initial rock mean horizontal permeability	$\overline{k_H}$	md	6
Initial rock mean vertical permeability	$\overline{k_V}$	md	6
Parameter of lognormal permeability distribution	σ_k	-	0.8
Initial rock mean specific surface area	$\overline{a_{v0}}$	m^{-1}	500
Mean initial pore radius	$\overline{r_{p0}}$	m	10^{-5}
Acid Density	ρ_b	kg/m^3	1040
Acid Dynamic viscosity	μ_b	cp	1
Initial Saturation	S_b	-	1
Inlet Acid Saturation	S_b	-	1
Acid molecular diffusivity	D_m	m^2/s	3.6×10^{-9}
Surface reaction-rate constant	k_s	m/s	0.015
Acid gravimetric dissolving power	β_{100}		1.37
Rock Mineral Density	ρ_m	kg/m^3	2710
Pore radius evolution parameter	γ	-	9
surface area evolution parameter	η	-	0.33
Permeability evolution parameter	δ	-	3

Table 4.3 Parameters for (a) fluid, (b) relative permeability, (c) capillary pressure

(a)						
Fluid	$\rho\ (kg/m^3)$	$\mu\ (Pa\ s)$				
Nitrogen	156	20.1×10^{-5}				
Oil	920	1×10^{-2}				
(b)						
Model	m_w	m_n	$S_{b,irr}$	$S_{a,irr}$	k_{ramax}	k_{rbmax}
Brooks and Corey (nitrogen)	4	3	0.18	0.001		
Brooks and Corey (oil)	3	2	0.18	0.1	0.8	0.3
(c)						
Model	α	p_{c0}				
Brooks and Corey	0.5	100				

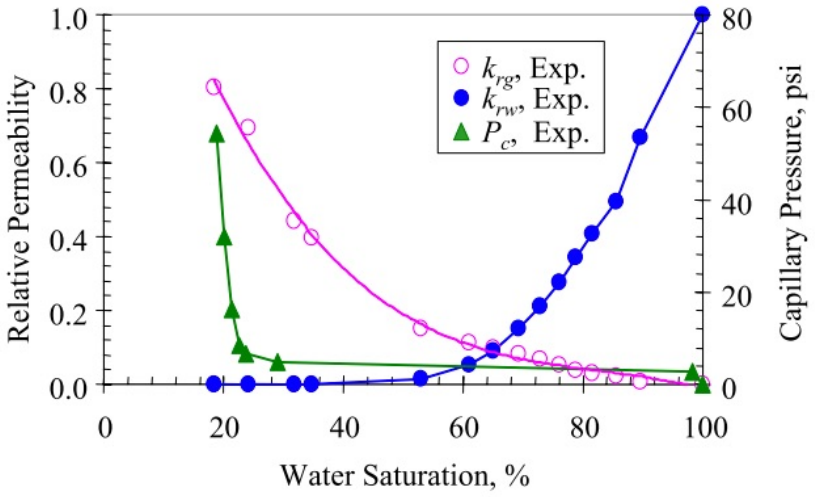

Figure 4.20 Experimental data of drainage nitrogen-water relative permeability and capillary pressure (Li and Horne, 2003)

The procedure for alternating injection is as follows:

1) Inject acid for 40s
2) Inject nitrogen for 40s
3) Inject acid for 20s
4) Inject nitrogen for 20s
5) Inject acid for 40s
6) Inject nitrogen for 20s
7) Inject acid to breakthrough

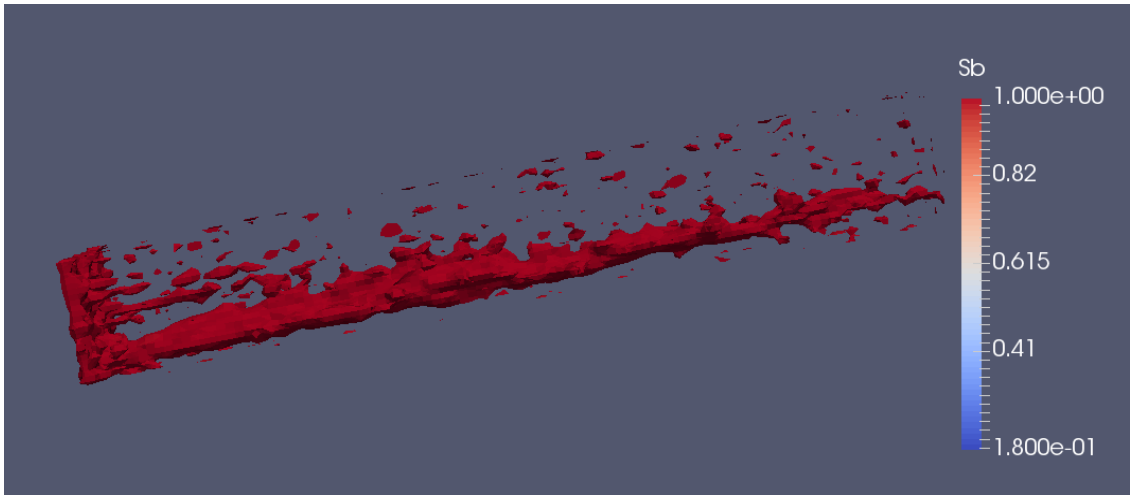

Figure 4.21 Acid injection into water saturated core

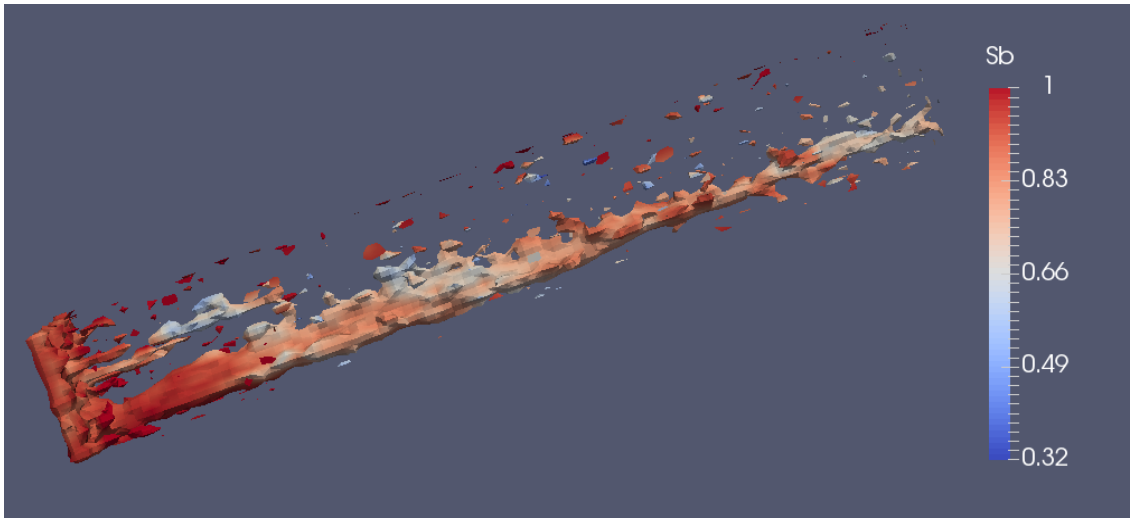

Figure 4.22 Alternating nitrogen/water injection

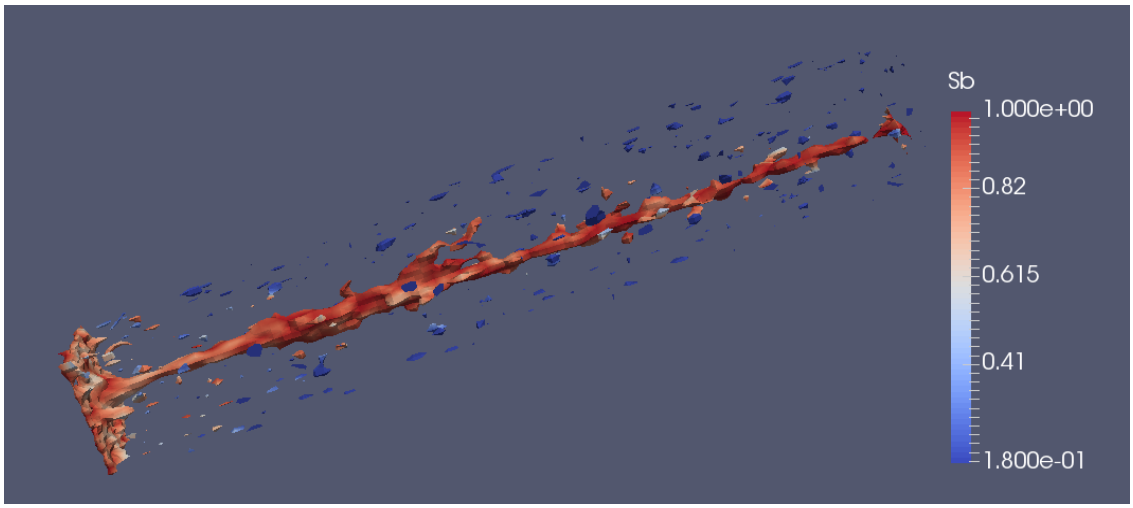

Figure 4.23 Acid injection into oil saturated core

The flow rate for the above cases is 5.8 mL/min. The wormhole structure is the volume of the porosity from 0.4 to 1. The color indicates acid saturation with blue as 0.18 (connate water saturation) and red as 1. The breakthrough time for the three cases is listed in **Table 4.4**.

Table 4.4 Simulation result

	injection rate (mL/min)	Breakthrough time (s)	breakthrough pore volume
Water saturated core	5.8	115	0.51
Alternate injection	5.8	125	0.56
Oil saturated core	5.8	65	0.29

In **Fig. 4.24**, the round dots represents the experimental results from Shukla's work (Shukla et al., 2003), triangle represents the simulation result. From **Fig. 4.21** and **4.22**, the wormhole generated using alternating gas/acid injection is not showing much difference on structure comparing with acid injecting into water saturated cores. The reason is that the picture is using volume of the porosity higher than 0.4, small branches cannot be seen from the image. However, the breakthrough pore volume needed for alternating gas/acid injection is higher than that for acid injection into water saturated cores. The wormhole generated with acid injection into the oil saturated core has the thinnest wormhole and the breakthrough pore volume is much lower. These results are consistent with lab experimental results and matched the experimental results quantitatively. It gives a better understanding when looking at different parameters separately.

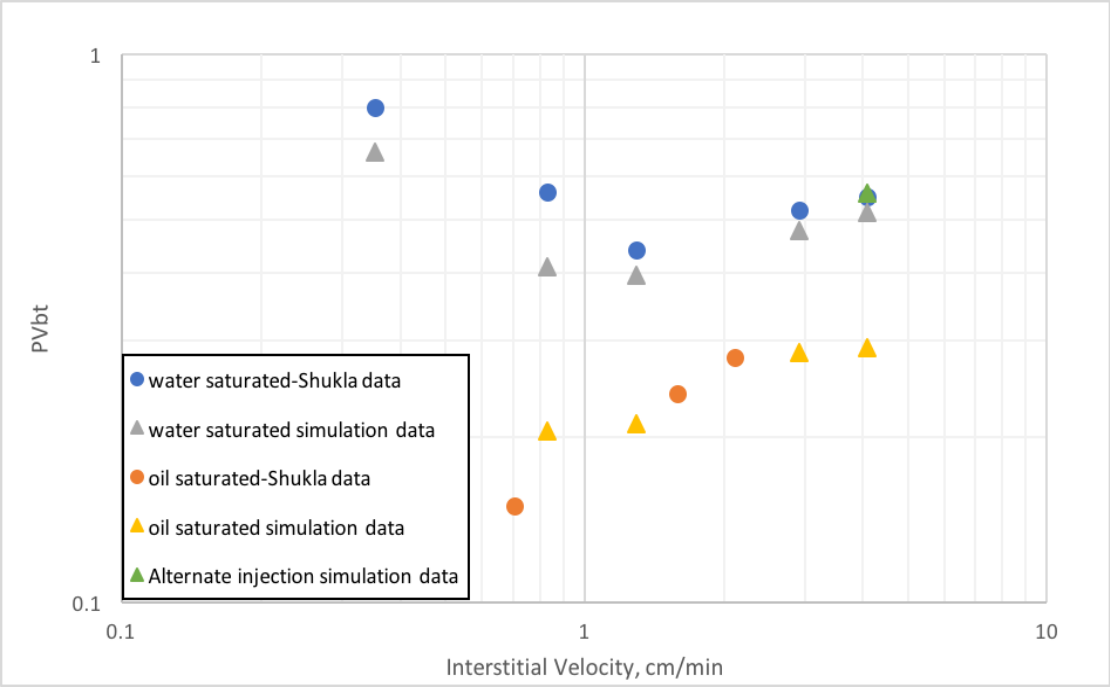

Figure 4.24 Experimental result and simulation result

4.11.3 Model limitations

The model shows good matching results with experimental data, however, limitation for the model should be noted. The parameter γ, η, δ are three tuning parameters used for matching the data, and cannot be measured in laboratory. They should be tuned for each rock with different properties, in order to better match the experimental data.

The mean specific surface area, $\overline{a_v}$, should also be regarded as a tuning parameter (Schwalbert et al., 2017). The specific surface area should be on the order of magnitude of $(1/r_p)$ or larger based on different pore structure, mode of packing and shape of the grains. However, in this study, the value of $\overline{a_{v0}}$ that better match the experimental data is much smaller than that of the theoretical value.

4.12 Chapter summary

In this chapter, we implement the porous multiphase solver and two-scale continuum model into *wormhole2PhFoam*, a 3-dimensional solver that can simulate the wormhole propagation in two-phase flow region.

And then, the model is validated in two cases: quantitatively matching the experimental data of single phase matrix acidizing and qualitatively matching the effect of acid injection into oil formation and alternating acid/gas injection in wormhole propagation.

5. RESULTS AND DISCUSSION

5.1 Introduction

In the previous chapters, the 3-D two-phase matrix acidizing simulator is used to predict single phase optimal condition and to simulate the alternate gas/acid injection process. In this chapter, the simulator is used to simulate the evolved CO_2 effect on wormhole propagation and a parametric study is conducted to investigate the parameters affecting wormhole propagation in two-phase flow region.

5.2 Evolved CO_2 effect simulation

The evolved CO_2 effect, as discussed in previous sections, can hinder wormhole propagation when presenting as gaseous or vapor phase at low injection rate. In order to simulate the evolved CO_2 effect. The mass rate of gaseous phase generation needs to be considered. Thus, Equation 4-8 is transferred to

$$m_a = \rho_a \Gamma_a R(C_s) = \frac{1}{2} a_v S_b \left(\frac{k_s k_c}{k_s + k_c}\right) C_b \frac{\rho_b}{M_{HCl}} M_{CO_2} \tag{5-1}$$

where M_{HCl} is the molecular weight of HCl, M_{CO_2} is the molecular weight of CO_2. $\Gamma_a = \frac{1}{2}$ based on the reaction. Based on Equation 5-1, the evolved CO_2 can be calculated based on the reaction between HCl and calcite. In this model, CO_2 density is assumed to be constant during the wormhole propagation process. This assumption is not accurate, as gaseous phase CO_2 density changes with pressure.

To simulate the problem, a 2-D domain is constructed, as shown in **Fig. 5.1**. The domain size is 0.2×0.04 m^2 (8000 computation cells with a 200×40 mesh). The porosity (**Fig. 5.2**) and permeability (**Fig. 5.3**) fields are populated using the same parameters as in the previous section to ensure the effectivity of tuning parameters. Acid is injected from the inlet at a constant rate.

The boundary conditions are as follows：

$$U_i = u_{i,0} \; at \; x = 0, \; i = a, b \tag{5-2}$$

$$\frac{\partial U_i}{\partial x} = 0 \; at \; x = L, \; i = a, b \tag{5-3}$$

$$S_b = 1 \;\; at \; x = 0 \tag{5-4}$$

$$C_f = C_0 \; at \; x = 0 \tag{5-5}$$

$$p = 0 \; at \; x = L \tag{5-6}$$

$$p|_{x=0} = \; p|_{y=0} = p|_{y=h} = [darcyGradPressure, \text{ fixed value} = 0] \tag{5-7}$$

$$\frac{\partial C_f}{\partial y} = 0 \; at \; y = 0 \; and \; y = h \tag{5-8}$$

The initial conditions are

$$S_b = 1 \; at \; t = 0 \tag{5-9}$$

$$U_i = 0 \; at \; t = 0 \tag{5-10}$$

$$C_f = 0 \; at \; t = 0 \tag{5-11}$$

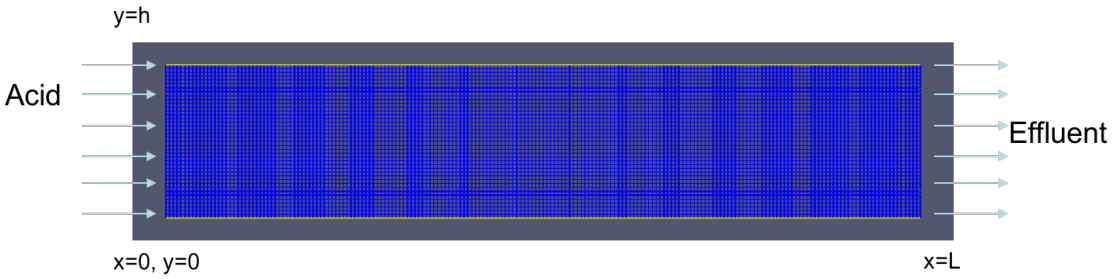

Figure 5.1 Schematic of 2D domain for the study

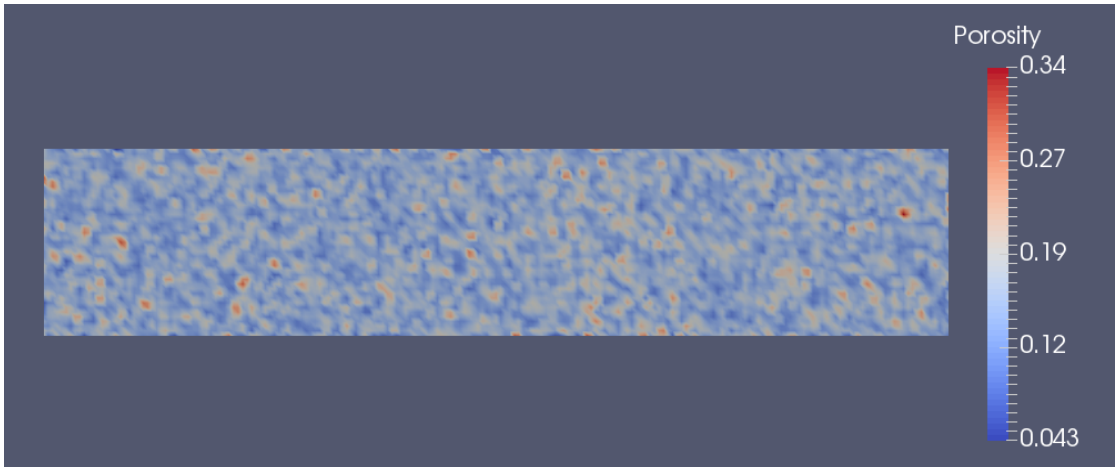

Figure 5.2 Porosity field of the domain

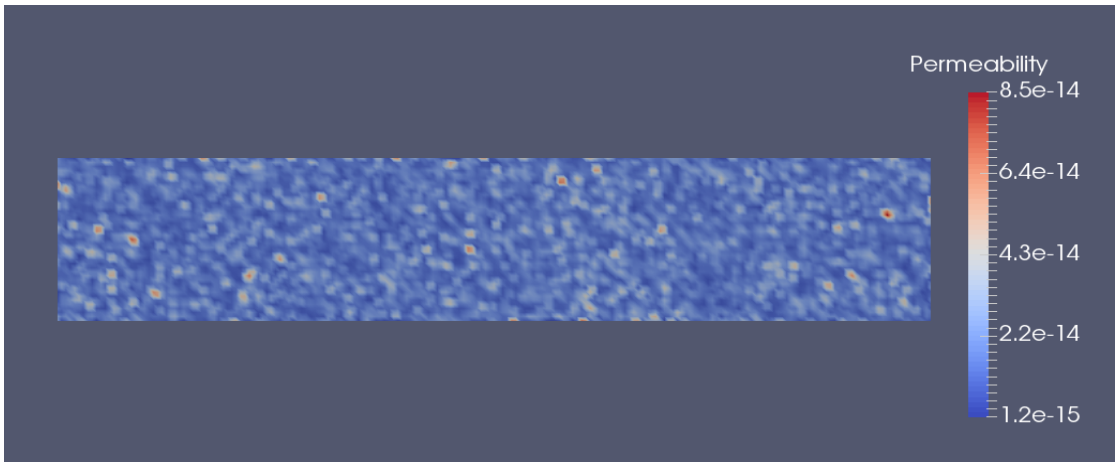

Figure 5.3 Permeability field of the domain, m^2

Two pressure conditions, 500 psi and 2000 psi are tested. The CO_2 properties under each condition are listed in **Table 5.1**.

Table 5.1 Evolved CO_2 properties under each condition

Pressure (psi)	Viscosity (10^{-5} pa•s)	Density (kg/m^3)
500	17.85	94.86
2000	43.16	563.05

The relative permeability and capillary pressure parameters are listed in **Table 5.2**. The other input parameters for the model are listed in **Table 5.3**.

Table 5.2 Parameters for: (a) relative permeability, (b) capillary pressure curve

(a)				
Model	m_n	m_w	$S_{b,irr}$	$S_{a,irr}$
Brooks and Corey	4	3	0.18	0.001
(b)				
Model	α		p_{c0}	
Brooks and Corey	0.5		100	

Table 5.3 Parameters used in this simulation

Parameters	Symbol	Units	Value
Core length	-	inch	8
Core height	-	inch	1.5
Initial rock mean porosity	ϕ_0	-	0.15
Parameter of lognormal porosity distribution	σ_ϕ	-	0.4
Initial rock mean horizontal permeability	$\overline{k_H}$	md	10
Initial rock mean vertical permeability	$\overline{k_V}$	md	10
Parameter of lognormal permeability distribution	σ_k	-	0.8
Initial rock mean specific surface area	$\overline{a_{v0}}$	m^{-1}	500
Acid Density	ρ_b	kg/m^3	1040
Acid Dynamic viscosity	μ_b	cp	1
water initial saturation	S_{b0}	-	1
Acid Saturation at inlet	S_b	-	calculated
Acid molecular diffusivity	D_m	m^2/s	3.6×10^{-9}
Surface reaction-rate constant	k_s	m/s	0.015
Acid gravimetric dissolving power	β_{100}		1.37
Rock Mineral Density	ρ_m	kg/m^3	2710
Pore radius evolution parameter	γ	-	8
surface area evolution parameter	η	-	0.33
Permeability evolution parameter	δ	-	3

Fig. 5.4 shows the wormhole structure at 75s with the injection rate of 1 ml/min under 500 psi and 2000 psi backpressure. The result shows that at the same time step, the wormhole under 500 psi propagates much faster than that of 2000 psi backpressure. This is not the same as what is observed in the lab experiment. Hindered wormhole propagation

is not captured using this model. **Fig. 5.5** shows the saturation map of the two backpressures. From the figure, we can see that as the density of CO_2 under 500 psi backpressure is much lower than that of 2000 psi backpressure, the generated CO_2 occupies larger volume in the domain. The water saturation under 500 psi backpressure is lower compared to that of 2000 psi backpressure. As the model is governed by Darcy's Law, the relative permeability of acid is lower and acid loss is lower in 500 psi backpressure case, resulting faster wormhole propagation.

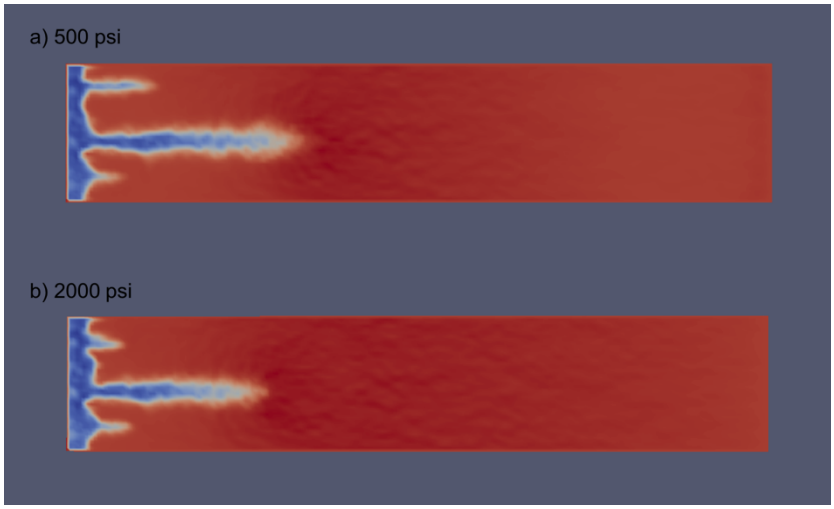

Figure 5.4 Wormhole structure at 75s at 1 ml/min injection under different backpressure

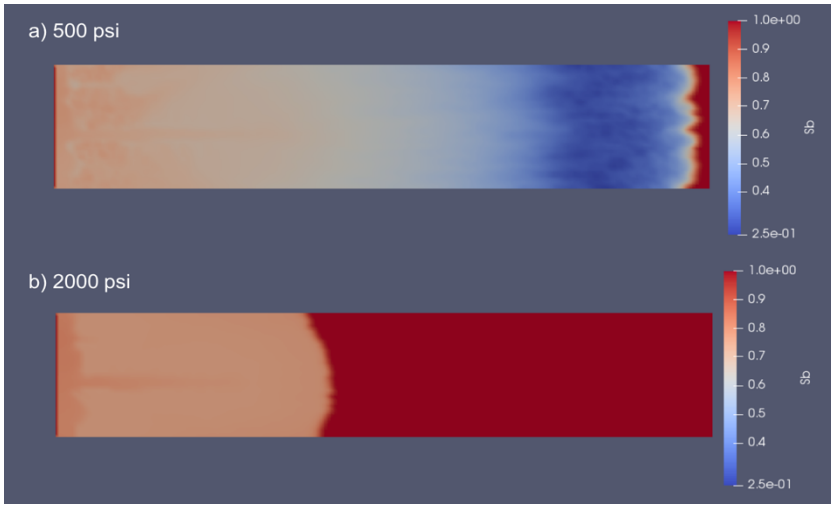

Figure 5.5 Saturation map at 75s at different backpressure

The reason that this model is not capturing the hindered wormhole effect at low backpressure, low injection rate, is that this model is using Darcy's Law as governing equation. Although the permeability inside the wormhole is much higher than that of the surrounding matrix, gas bubble gathering and blockage cannot be described using Darcy's Law. In order to simulate the evolved CO_2 effect, Navier-Stokes equation should be used.

5.3 Parametric study of two-phase effect

In this section, a parametric study of two-phase flow effect is conducted by simulating acid injection into oil formation. Although the model cannot be used to simulate evolved CO_2 effect, it can still be used to simulate acid injection into oil formation. As in real field application, the evolved CO_2 is not likely to present as a gaseous phase, the effect of evolved CO_2 is negligible. Parameters such as oil viscosity, residue oil saturation, initial water saturation are investigated. The simulation is conducted using the same domain as

in section 4.11.2. The parameters for the simulation are listed in **Table 4.2**. The base case oil properties and relative permeability parameters for typical water wet reservoir are listed in **Table 5.5**. The relative permeability curve is shown in **Fig. 5.6**. Capillary pressure is neglected in this study.

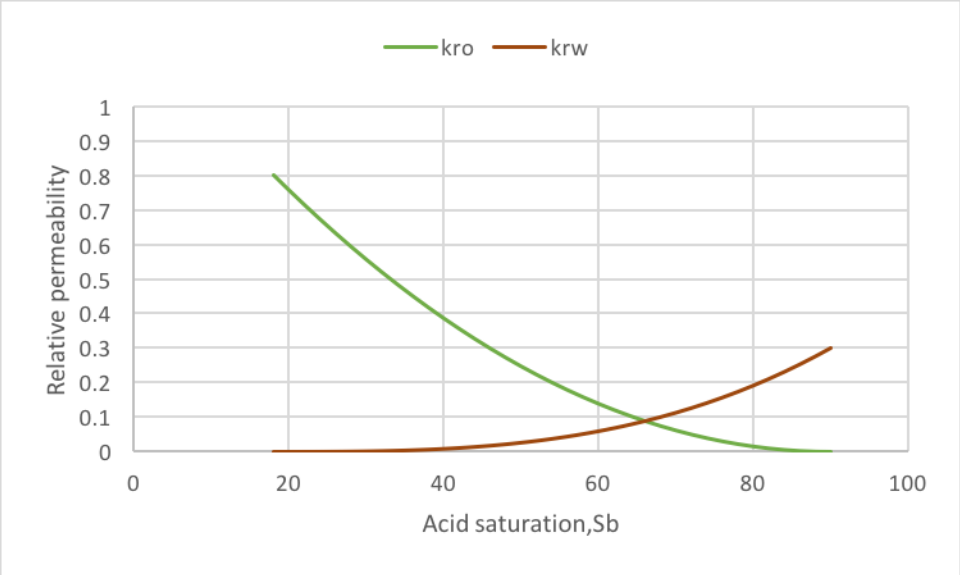

Figure 5.6 Relative permeability curve for typical water wet reservoir

Table 5.4 Parameters for: (a) oil, (b) relative permeability

(a)						
Fluid	$\rho\ (kg/m^3)$	$\mu\ (Pa\ s)$				
Oil	920	1×10^{-2}				
(b)						
Model	m_w	m_n	$S_{b,irr}$	$S_{a,irr}$	k_{ramax}	k_{rbmax}
Brooks and Corey	3	2	0.18	0.1	0.8	0.3

5.3.1 Effect of oil viscosity

Figure 5.7 shows the effect of oil viscosity on wormhole efficiency. The grey triangles are the results of acid injection into water saturated cores. The blue dots and yellow dots are the simulation results for acid injection into oil saturated cores with viscosity of 2 cp and 10 cp respectively. From the results, we can see high oil viscosity reduce acid consumption and lower optimal breakthrough pore volume.

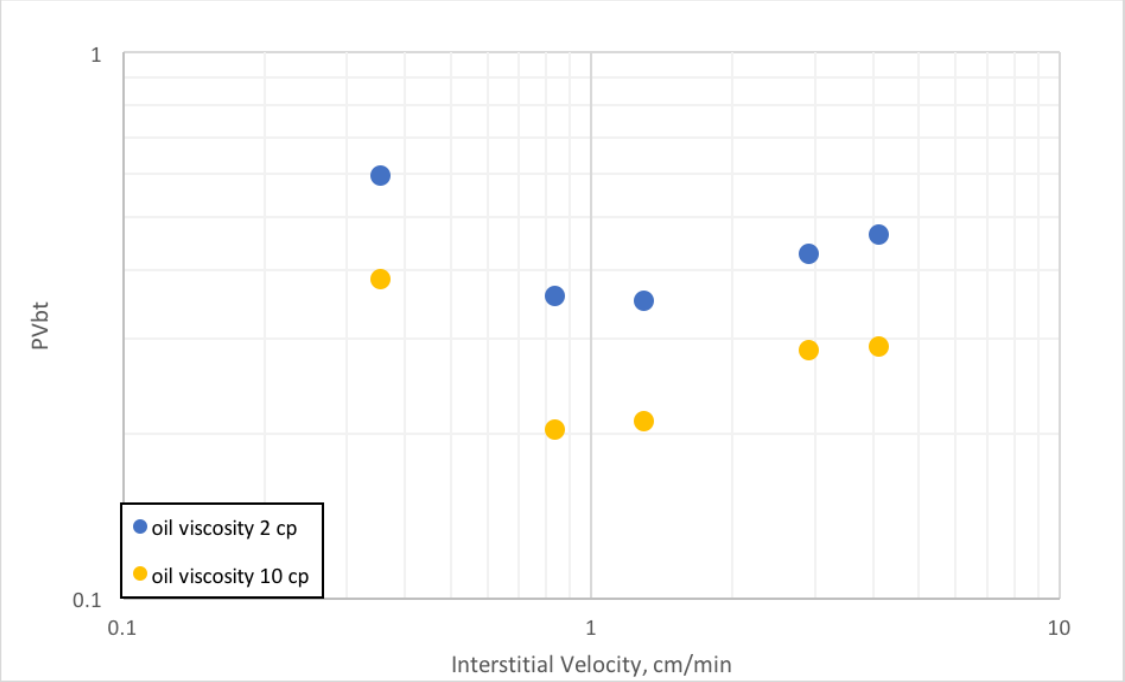

Figure 5.7 Effect of oil viscosity

5.3.2 Effect of residue oil saturation

Residue oil saturation is the fraction of pore volume occupied by oil at the end of oil displacement. For different kinds of reservoirs, the residue oil saturation is different. In

this section, three different residue oil saturations, $S_{a,irr} = 0.1$, $S_{a,irr} = 0.2$, and $S_{a,irr} = 0.3$ are simulated.

From the results, we can see that as the residue oil saturation increases, the breakthrough pore volume decreases (**Fig. 5.8**). As the residue oil saturation increases, the pore space for acid transport is reduced. For the same injection rate, the pore volume of oil which can be displaced by the acid fluid is reduced, resulting in faster acid breakthrough.

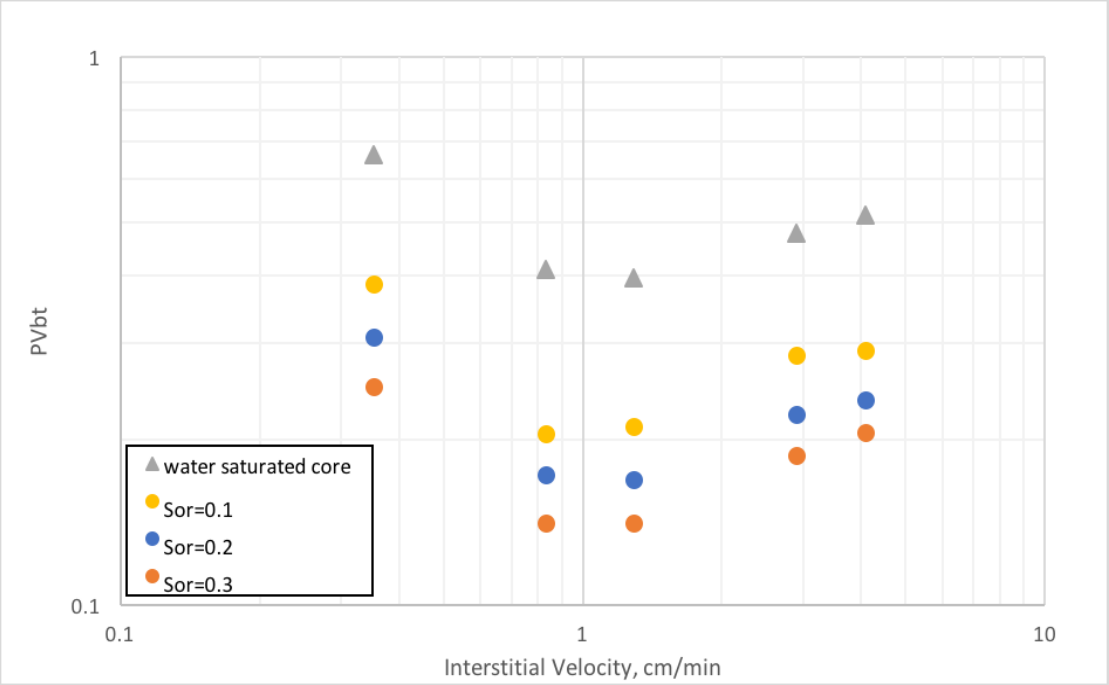

Figure 5.8 Effect of residue oil saturation

5.3.3 Effect of initial water saturation

Assuming the reservoir is water-wet with relative permeability properties as shown in **Fig. 5.6**. Initial water saturation may be different at different location of the reservoir. Three different initial water saturation values are tested: (1) $S_{w0} = 0.18$, conate water saturation, (2) $S_{w0} = 0.4$, (3) $S_{w0} = 0.9$, with residue oil saturation.

The simulation results are plotted in **Fig. 5.9**. From the simulation results, we can see that the breakthrough pore volume needed for $S_{w0} = 0.9$, residue oil saturation is slightly lower than that of single-phase matrix acidizing. As the initial water saturation decreases, the breakthrough pore volume decreases. The presence of oil phase in the core, reduces the acid leakoff on the wormhole wall and promotes wormhole propagation.

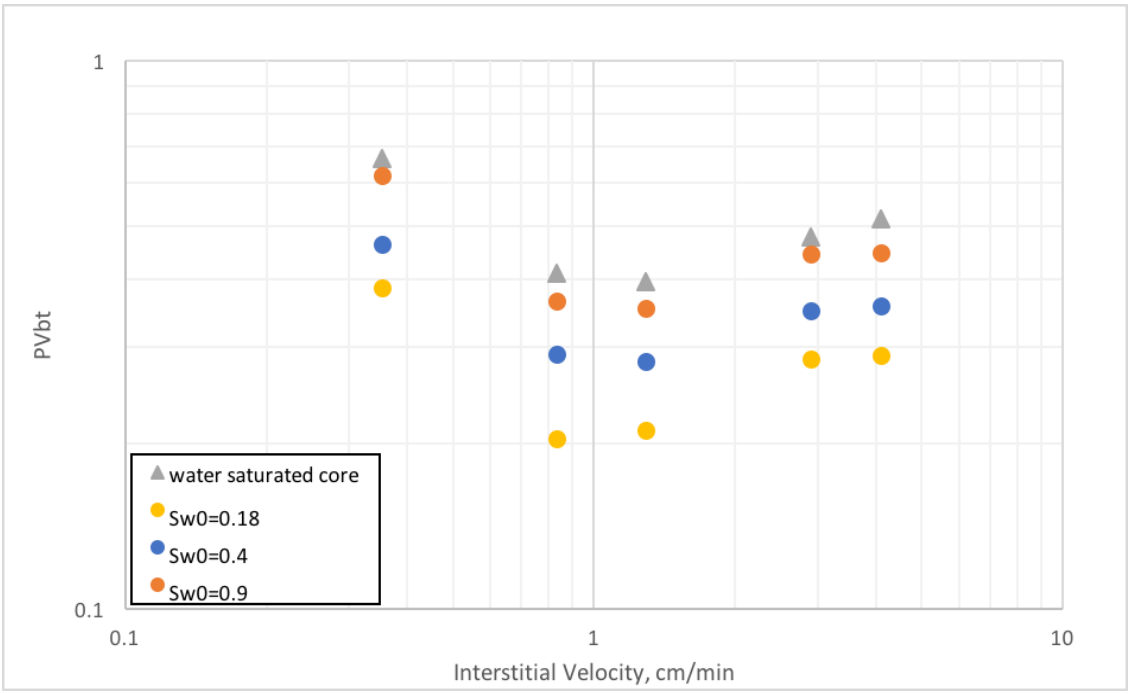

Figure 5.9 Effect of initial water saturation

6. CONCLUSIONS

This study presents an integrated experimental and numerical study of two-phase flow effect on matrix acidizing. Laboratory core flooding experiments were done using 1.5-inch by 8-inch Indiana limestone cores under different temperature and backpressures to investigate the evolved CO_2 effect on wormhole propagation.

A 3-D two-phase matrix acidizing simulator is constructed with two-scale continuum model and finite volume method to characterize matrix acidizing process. The model can capture both gravity effect and two-phase flow effect on wormhole propagation.

Important developments and conclusions can be summarized as:

1. At the injection rates lower than the optimal rate, gaseous CO_2 in the system lowers the wormhole propagation rate and enlarges the wormhole diameter.
2. When the injection rate creates fluxes that are greater than the optimal interstitial velocity, the negative effect of CO_2 on wormhole propagation diminishes at lower temperature (70ºF) and disappears at higher temperature (150ºF).
3. CO_2 present as liquid phase or supercritical phase does not have a significant effect on wormholing behavior.
4. Darcy's Law cannot be used to simulated the evolved CO_2 effect during matrix acidizing process.
5. The effect of different parameters affecting two-phase wormhole propagation is studied. The presence of an immiscible phase, such as gas or oil, before acid

injection, can increase the wormholing efficiency. The higher the oil viscosity, the lower volume of acid needed for wormhole penetrating the core. A higher initial saturation of oil, also reduces the breakthrough pore volume. High residue oil saturation has a positive effect on wormholing efficiency.

6. This study shows us wormhole propagation in two-phase flow region is quite different with single-phase flow. It is important to investigate the effects and calibrate the lab results before using them in oil and gas reservoirs.

REFERENCES

Akanni, O. O., and Nasr-El-Din, H. A., 2015, The Accuracy of Carbonate Matrix-Acidizing Models in Predicting Optimum Injection and Wormhole Propagation Rates. In SPE Middle East Oil & Gas Show and Conference. Society of Petroleum Engineers.

Akanni, O. O., and Nasr-El-Din, H. A., 2016, Modeling of Wormhole Propagation During Matrix Acidizing of Carbonate Reservoirs by Organic Acids and Chelating Agents. In SPE Annual Technical Conference and Exhibition. Society of Petroleum Engineers

Anderson, T. B., and Jackson, R., 1967, Fluid Mechanical Description of Fluidized Beds. Equations of Motion. Industrial & Engineering Chemistry Fundamentals, 6(4), 527-539.

Bernadiner, M. G., Thompson, K. E., and Fogler, H. S., 1992, Effect of Foams Used During Carbonate Acidizing. SPE Production Engineering, 7(04), 350-356.

BP, 2016, BP Statistical Review of World Energy 2016: no. June, p. 1–48.

Brinkman, H. C., 1949, A Calculation of the Viscous Force Exerted by a Flowing Fluid on a Dense Swarm of Particles. Applied Scientific Research, 1(1), 27-34

Brooks, R. H., and Corey, A. T., 1964, Hydraulic Properties of Porous Media: Hydrology Papers. Colorado State University, 24.

Buijse, M. A., 1997, Mechanisms of Wormholing in Carbonate Acidizing. In International Symposium on Oilfield Chemistry. Society of Petroleum Engineers.

Buijse, M. A., and Glasbergen, G., 2005, A Semi-Empirical Model to Calculate Wormhole Growth in Carbonate Acidizing. In SPE Annual Technical Conference and Exhibition. Society of Petroleum Engineers.

Cheng, H., Zhu, D., and Hill, A. D., 2017, The Effect of Evolved CO2 on Wormhole Propagation in Carbonate Acidizing. SPE Production & Operations, 32(03), 325-332.

Civan, F., 2000, Predictability of Porosity and Permeability Alterations by Geochemical and Geomechanical Rock and Fluid Interactions. In SPE International Symposium on Formation Damage Control. Society of Petroleum Engineers.

Daccord, G., 1987, Chemical Dissolution of a Porous Medium by a Reactive Fluid. Physical Review Letters, 58(5), 479.

Daccord, G., Touboul, E., and Lenormand, R., 1989, Carbonate Acidizing: Toward a Quantitative Model of the Wormholing Phenomenon. SPE Production Engineering, 4(01), 63-68.

Daccord, G., Lenormand, R., and Lietard, O., 1993, Chemical Dissolution of a Porous Medium by a Reactive Fluid - I. Model for the "Wormholing" Phenomenon. Chemical Engineering Science, 48(1), 169-178.

De Oliveira, T. J. L., De Melo, A. R., Oliveira, J. A. A., and Pereira, A. Z., 2012, Numerical Simulation of the Acidizing Process and PVBT Extraction Methodology Including Porosity/Permeability and Mineralogy Heterogeneity. In SPE International Symposium and Exhibition on Formation Damage Control. Society of Petroleum Engineers.

Dong, K., Jin, X., Zhu, D., and Hill, A. D., 2014, The Effect of Core Dimensions on the Optimal Acid Flux in Carbonate Acidizing. In SPE International Symposium and Exhibition on Formation Damage Control. Society of Petroleum Engineers.

Dong, K., 2015, Theoretical and Experimental Study on Optimal Conditions in Carbonate Acidizing. Doctoral dissertation, Texas A&M University.

Dubetz, D., Cheng, H., Zhu, D., and Hill, A. D., 2016, Characterization of Rock Pore Size Distribution and its Effects on Wormhole Propagation. In SPE Annual Technical Conference and Exhibition. Society of Petroleum Engineers.

El-Amin, M. F., Meftah, R., Salama, A., and Sun, S., 2015, Numerical Treatment of Two-Phase Flow in Porous Media including Specific Interfacial Area. Procedia Computer Science, 51, 1249-1258.

Fredd, C. N., and Fogler, H. S., 1998, Influence of Transport and Reaction on Wormhole Formation in Porous Media. AIChE Journal, 44(9), 1933-1949.

Fredd, C. N., and Fogler, H. S., 1999, Optimum Conditions for Wormhole Formation in Carbonate Porous Media: Influence of Transport and Reaction. SPE Journal, 4(03), 196-205.

Furui, K., Burton, R. C., Burkhead, D. W., Abdelmalek, N. A., Hill, A. D., Zhu, D., and Nozaki, M., 2012, A Comprehensive Model of High-rate Matrix Acid Stimulation for Long Horizontal Wells in Carbonate Reservoirs: Part I--Scaling Up Core-level Acid Wormholing to Field Treatments. SPE Journal, 17(01), 271-279.

Gdanski, R., 1999, A Fundamentally New Model of Acid Wormholing In Carbonates. In European Formation Damage Conference (pp. 107-116).

Golfier, F., Bazin, B., Zarcone, C., Lernormand, R., Lasseux, D., and Quintard, M., 2001, Acidizing Carbonate Reservoirs: Numerical Modelling of Wormhole Propagation and Comparison to Experiments. In SPE European Formation Damage Conference. Society of Petroleum Engineers.

Golfier, F., Zarcone, C., Bazin, B., Lenormand, R., Lasseux, D., and Quintard, M., 2002, On the Ability of a Darcy-Scale Model to Capture Wormhole Formation During the Dissolution of a Porous Medium. Journal of Fluid Mechanics, 457, 213-254.

Golfier, F., Bazin, B., Lenormand, R., and Quintard, M., 2004, Core-scale Description of Porous Media Dissolution During Acid Injection - Part I: Theoretical Development. Computational & Applied Mathematics, 23(2-3), 173-194.

Gong, M., and El-Rabaa, A. M., 1999, Quantitative Model of Wormholing Process in Carbonate Acidizing. In SPE Mid-Continent Operations Symposium. Society of Petroleum Engineers.

Grabski, E., 2012, Matrix Acidizing Core Flooding Apparatus: Equipment and Procedure Description (Doctoral dissertation).

Grathwohl, P., 2012, Diffusion in Natural Porous Media: Contaminant Transport, Sorption/Desorption and Dissolution Kinetics (Vol. 1). Springer Science & Business Media.

Hall, M. J., and Hiatt, J. P., 1996, Measurements of Pore Scale Flows within and Exiting Ceramic Foams. Experiments in Fluids, 20(6), 433-440.

Hoefner, M. L., and Fogler, H. S., 1987, Role of Acid Diffusion in Matrix Acidizing of Carbonates. Journal of Petroleum Technology, 39(02), 203-208.

Hoefner, M. L., and Fogler, H. S.,1988, Pore Evolution and Channel Formation During Flow and Reaction in Porous Media. AIChE Journal, 34(1), 45-54.

Hoefner, M. L., and Fogler, H. S., 1989, Fluid-velocity and reaction-rate effects during carbonate acidizing: application of network model. SPE Production Engineering, 4(01), 56-62.

Horgue, P., Soulaine, C., Franc, J., Guibert, R., and Debenest, G., 2015, An Open-source Toolbox for Multiphase Flow in Porous Media. Computer Physics Communications, 187, 217-226.

Huang, T., Hill, A. D., and Schechter, R. S., 1997, Reaction Rate and Fluid Loss: The Keys to Wormhole Initiation and Propagation in Carbonate Acidizing. In International Symposium on Oilfield Chemistry. Society of Petroleum Engineers.

Huang, T., Zhu, D., and Hill, A. D., 1999, Prediction of Wormhole Population Density in Carbonate Matrix Acidizing. In European Formation Damage Conference (pp. 161-167).

Hung, K. M., Hill, A. D., and Sepehrnoori, K., 1989, A Mechanistic Model of Wormhole Growth in Carbonate Matrix Acidizing and Acid Fracturing. Journal of Petroleum Technology, 41(01), 59-66.

Izgec, O., Zhu, D., and Hill, A. D., 2009, Models and Methods for Understanding of Early Acid Breakthrough Observed in Acid Core-Floods of Vuggy Carbonates. In 8th European Formation Damage Conference. Society of Petroleum Engineers.

Kalia, N., and Balakotaiah, V., 2007, Modeling and Analysis of Wormhole Formation in Reactive Dissolution of Carbonate Rocks. Chemical Engineering Science, 62(4), 919-928.

Kalia, N., 2008, Modeling and analysis of reactive dissolution of carbonate rocks. Dissertations & Theses - Gradworks, 8(2), 67-151.

Kalia, N., and Balakotaiah, V., 2009, Effect of Medium Heterogeneities on Reactive Dissolution of Carbonates. Chemical Engineering Science, 64(2), 376-390.

Krevor, S., Pini, R., Zuo, L., and Benson, S. M., 2012, Relative Permeability and Trapping of CO2 and Water in Sandstone Rocks at Reservoir Conditions. Water Resources Research, 48(2).

Li, K., and Horne, R. N., 2003, A Wettability Evaluation Method for Both Gas-Liquid-Rock and Liquid-Liquid-Rock Systems. In International Symposium on Oilfield Chemistry. Society of Petroleum Engineers.

Liu, M., Zhang, S., and Mou, J., 2012, Fractal Nature of Acid-Etched Wormholes and The Influence of Acid Type on Wormholes. Petroleum Exploration and Development, 39(5), 630-635.

Liu, M., Zhang, S., Mou, J., and Zhou, F., 2013, Wormhole Propagation Behavior under Reservoir Condition in Carbonate Acidizing. Transport in Porous Media, 96(1), 203-220.

Liu, X., and Ortoleva, P., 1996, A General-Purpose, Geochemical Reservoir Simulator. In SPE Annual Technical Conference and Exhibition. Society of Petroleum Engineers.

Maheshwari, P., and Balakotaiah, V., 2013, Comparison of Carbonate HCl Acidizing Experiments with 3D Simulations. SPE Production & Operations, 28(04), 402-413.

Maheshwari, P., Ratnakar, R. R., Kalia, N., and Balakotaiah, V., 2013, 3-D Simulation and Analysis of Reactive Dissolution and Wormhole Formation in Carbonate Rocks. Chemical Engineering Science, 90, 258-274.

Marle, C. M., 1982, On Macroscopic Equations Governing Multiphase Flow with Diffusion and Chemical Reactions in Porous Media. International Journal of Engineering Science, 20(5), 643-662.

McDuff, D., Shuchart, C. E., Jackson, S., Postl, D., and Brown, J. S., 2010, Understanding Wormholes in Carbonates: Unprecedented Experimental Scale and 3-D Visualization. In SPE Annual Technical Conference and Exhibition. Society of Petroleum Engineers.

Moukalled, F., Mangani, L., and Darwish, M., 2016, The Finite Volume Method in Computational Fluid Dynamics. Fluid Mechanics & Its Applications, 29(1), 3–38.

Mumallah, N. A., 1991, Factors Influencing the Reaction Rate of Hydrochloric Acid and Carbonate Rock. In SPE International Symposium on Oilfield Chemistry. Society of Petroleum Engineers.

Mumallah, N. A., 1996, Hydrochloric Acid Diffusion Coefficients at Acid-Fracturing Conditions. Journal of Petroleum Science and Engineering, 15(2-4), 361-374.

Muskat, M., Wyckoff, R. D., Botset, H. G., and Meres, M. W., 1937, Flow of Gas-Liquid

Mixtures through Sands. Transactions of the AIME, 123(01), 69-96.

Ott, H., and Oedai, S., 2015, Wormhole Formation and Compact Dissolution in Single- and Two-Phase CO2-Brine Injections. Geophysical Research Letters, 42(7), 2270-2276.

Panga, M. K., Balakotaiah, V., and Ziauddin, M., 2002, Modeling, Simulation and Comparison of Models for Wormhole Formation During Matrix Stimulation of Carbonates. In SPE Annual Technical Conference and Exhibition. Society of Petroleum Engineers.

Panga, M. K. R., 2003, Multiscale transport and reaction: two case studies (Doctoral dissertation, University of Houston).

Panga, M. K., Ziauddin, M., and Balakotaiah, V., 2005, Two-Scale Continuum Model for Simulation of Wormholes in Carbonate Acidization. AIChE Journal, 51(12), 3231-3248.

Pomès, V., Bazin, B., Golfier, F., Zarcone, C., Lenormand, R., and Quintard, M., 2001, On the Use of Upscaling Methods to Describe Acid Injection in Carbonates. In SPE Annual Technical Conference and Exhibition. Society of Petroleum Engineers.

Prutton, C. F., and Savage, R. L., 1945, The Solubility of Carbon Dioxide in Calcium Chloride-Water Solutions at 75, 100, 120 and High Pressures. Journal of the American Chemical Society, 67(9), 1550-1554.

Qiu, X., Zhao, W., Chang, F., and Dyer, S., 2013, Quantitative Modeling of Acid Wormholing in Carbonates-What Are the Gaps to Bridge. In SPE Middle East Oil and Gas Show and Conference. Society of Petroleum Engineers.

Qiu, X. W., Zhao, W., Dyer, S. J., Al Dossary, A., Khan, S., and Sultan, A. S., 2014, Revisiting Reaction Kinetics and Wormholing Phenomena During Carbonate Acidizing. In IPTC 2014: International Petroleum Technology Conference.

Quintard, M., and Whitaker, S., 1999, Dissolution of An Immobile Phase During Flow in Porous Media. Industrial & Engineering Chemistry Research, 38(3), 833-844.

Ratnakar, R., Kalia, N., and Balakotaiah, V., 2012, Carbonate Matrix Acidizing with Gelled Acids: An Experiment-Based Modeling Study. In SPE International Production and Operations Conference & Exhibition. Society of Petroleum Engineers.

Schechter, R. S., and Gidley, J. L., 1969, The Change in Pore Size Distribution from Surface Reactions in Porous Media. AIChE Journal, 15(3), 339-350.

Schechter, R. S., 1992, Oil Well Stimulation: Old Tappan, NJ (United States); Prentice Hall Inc.

Schwalbert, M. P., Zhu, D., and Hill, A. D., 2017, Extension of an Empirical Wormhole Model for Carbonate Matrix Acidizing Through Two-Scale Continuum 3D Simulations. In SPE Europec featured at 79th EAGE Conference and Exhibition. Society of Petroleum Engineers.

Sheldon, J. W., and Cardwell Jr, W. T., 1959, One-dimensional, Incompressible, Noncapillary, Two-Phase Fluid Flow in a Porous Medium.

Shukla, S., Zhu, D., and Hill, A. D., 2003, Gas Assisted Acidizing of Carbonate Formations. In SPE European Formation Damage Conference. Society of Petroleum Engineers.

Soulaine, C., and Tchelepi, H. A., 2016, Micro-Continuum Approach for Pore-Scale Simulation of Subsurface Processes. Transport in Porous Media, 113(3), 431-456.

Wang, Y., Hill, A. D., and Schechter, R. S., 1993, The Optimum Injection Rate for Matrix Acidizing of Carbonate Formations. In SPE Annual Technical Conference and Exhibition. Society of Petroleum Engineers.

Ward, V. L., 1986, N2 and CO2 in the Oil Field: Stimulation and Completion Applications (includes associated paper 16050). SPE Production Engineering, 1(04), 275-278.

Zakaria, A. S., Nasr-El-Din, H. A., and Ziauddin, M., 2015, Predicting the Performance of the Acid-Stimulation Treatments in Carbonate Reservoirs with Nondestructive Tracer Tests. SPE Journal, 20(06), 1-238.

Ziauddin, M. E., and Bize, E., 2007, The Effect of Pore Scale Heterogeneities on Carbonate Stimulation Treatments. In SPE Middle East Oil and Gas Show and Conference. Society of Petroleum Engineers.